The Defining Role of Local Shear on the Development of As-Rolled Microstructure and Crystallographic Texture in Steel

Saurabh Kumar[1], Sanjay Manda[1], Ujjal Tewary[1,2], Sivasambu Mahesh[3], R. Balamuralikrishnan[4], Rahul Kumar Verma[5], Manjini Sambandam[6], Shyamprasad Karagadde[7], Indradev Samajdar[1, *]

[1]Department of Metallurgical Engineering and Materials Science, IIT Bombay, Mumbai, 400076, India

[2]John Deere India Private Limited, Pune,411013, India

[3]Department of Aerospace Engineering, IIT Madras, Chennai, 600036, India

[4]Defence Metallurgical Research Laboratory, DRDO, Hyderabad, 500076, India

[5]Research and Development Divison, Tata Steel Ltd, Jamshedpur, 8310103, India

[6]Research and Development Division, JSW Steel Limited, Bellary, 583275, India

[7]Department of Mechanical Engineering, IIT Bombay, Mumbai, 400076, India

Abstract

This study involved laboratory unidirectional (UDR) and reverse (RR) cold rolling of steel, and corresponding direct (and indirect) observations of surface (and sub-surface) microstructures. Though both processes had identical strain mode of plane strain compression (PSC), the as-rolled surface grains showed clear differences in imposed mesoscopic shear strains. Further, the surface microstructure and its orientation sensitivity differed remarkably between the two processes. RR had more dislocation density, grain misorientations and non-crystallographic microbands, but exhibited insignificant differences between different crystallographic orientations. These effects appeared significant in low carbon interstitial free (IF) steel, but noticeably less so for high strength low alloy (HSLA) grade. The crystallographic textures of both the processes were identical in the mid-thickness section. However, the surface textures differed noticeably irrespective of the steel grade. These were captured quantitatively with a crystal plasticity model, and by introducing parametrically positive (UDR) and negative (RR) local shear strains for the respective surfaces. In summary, this study established, quantitatively, the defining role of local shear strain on the developments of as-rolled microstructure and crystallographic texture of steel.

Keywords: Rolling, Shear, Microstructure, Texture, Modelling.

*Corresponding author: indra@iitb.ac.in

1. Introduction

Rolling is, arguably, the most conventional but extensively used metal forming process[1–5]. Naturally, there are modifications to the traditional rolling practice. These range from shape rolling to asymmetric and special rolling techniques[1,6–8].The changes in the mill design have even been used to impart severe plastic deformation[2,9–11].·It appears that introduction of shear strains into the original plane strain compression (PSC) strain mode can be exploited effectively[12–18]. Redundant shear strain tends to have significant effect on dislocation substructure evolution, which arguably gets altered with rearrangement of dislocations[19–26]. In spite of all such present and potential applications, however, the role of local or redundant shear into the PSC strain tensor has never been subjected to focused and comprehensive microstructural evaluation. This has been the motivation behind the present study.

Even the traditional cold rolling is conducted in a tandem or reversible mill[2,4]. These are generalized, in this study, as unidirectional (UDR) and reversible (RR) cold rolling in a laboratory rolling mill. In addition to changes in rolling mill design and roll-pass schedule plus roll bite[27–35], even UDR or RR were reported to affect as-rolled microstructures and properties[33,36]. Rather than a speculative explanation from dislocation dynamics[37,38], the logical explanation has to exist within the purview of imposed strain – especially the local or redundant shear. The latter, arguably, may affect developments in as-rolled surface microstructures and crystallographic textures[17,31,39–48]. Disintegration of dislocation substructures with the dissolution of well-developed dislocation walls are expected outcome of changing the strain path[20,24,49–54] or strain mode, which in turn would affect the orientation sensitivity of plastic deformation[27,28,51]. However, alteration of dislocation substructure during changing of rolling mode due to inversion of shear strain tensor and its subsequent effects on crystallographic texture and orientation dependent dislocation density has rarely been touched.

Capturing these quantitatively, and modelling the developments in surface crystallographic textures with continuum plasticity constituted the twin objectives of this study.

This study used UDR and RR, in a laboratory cold rolling mill, of two steel grades. These were commercial hot-rolled, but fully recrystallized, interstitial free (IF), and high strength low alloy (HSLA) steels. Direct experimental observations quantified all aspects of as-rolled surface microstructure and crystallographic texture. The latter was then simulated with a continuum binary-tree model[55]. In particular, a parametric study on imposed local shear strain was designed to bring out the difference, if any, in local or redundant shear strain between UDR and RR cold rolling processes.

2. Experimental Procedure and Modelling Framework

2.1 Experimental Procedure

Commercial (from Tata™ Steel, India) hot rolled but fully recrystallized interstitials free (IF) and high strength low alloy (HSLA) steels were used as the starting material. The chemical compositions of the respective grades are given in Table I. These were cold rolled, total PSC strains imposed varied between ε = 0.2-0.6, in a laboratory rolling mill, Bühler™. As shown in Figure 1a, two rolling schedules of UDR and RR were used. It is to be noted that the roller diameter (150 mm) and initial sample dimensions (5 mm thickness) were kept identical between the two processes. In UDR, specimens were subjected to the same strain (ε = 0.05) in each pass by rolling in the same direction. In RR, on the other hand, the samples were rotated 180° to rolling direction (RD) after each successive pass of ε = 0.05. We have used laser engraved 3 mm diameter circles (Figure 1b) to measure macroscopic strain at the surfaces (T0). As shown in the Figure, and as expected, the circles became ellipses after rolling. These change in dimensions represented the major strain, which appeared identical between UDR and RR (see Figure 1b). Of course, the movement of material points[2] were different between the two processes. This appeared on the vertical marker lines. As UDR represented movement in only one direction, the vertical marker line appeared 'bent'. This was not the case for RR, due to reversal of sample (180º) after every pass.

Detailed microstructural characterizations were performed for the progressively cold rolled, UDR as well as RR, samples. These included direct observations on the same surface grains before and after the rolling, see Figure 1c. It is to be noted that use of very thin Teflon sheets were necessary to avoid surface defects and scratches on the electropolished surface grains. Further, the characterizations also involved as-rolled sub-surfaces, but these were indirect or statistical in nature.

The sample preparation for all characterizations involved standard metallography followed by electropolishing. In particular, an electrolyte of methanol and perchloric acid (in 80:20 ratio) was used. The electropolishing was conducted at 20 volts dc and 253K. Electron backscattered diffraction (EBSD) and X-ray diffraction (XRD) involved electropolishing with a Struers™ Lectropol-5. Transmission electron microscopy (TEM) samples, on the other hand, were made in a Struers™ Tenupol-5, a twin-jet electropolisher. A TSL-EDAX™ OIM™ system, on a FEI™ Quanta-3D field emission gun (FEG) scanning electron microscope (SEM), was used for our EBSD measurements. The same system was also employed for transmission Kikuchi diffraction (TKD). TEM observation were made in a Thermofisher™ Themis-300 transmission electron microscope. Beam and video conditions were kept identical for the EBSD and TKD scans. This study also used XRD for bulk crystallographic texture and residual strain measurements through a PanAlytical™ Empyrean system. Texture analysis was conducted with MTex™ and MTM-FHM™ software[56,57]. Residual strain analysis, on the other hand, was conducted with a commercial software - Xpert Stress Plus™. For further details on texture[58] and residual strain measurements and analysis[59–61], the reader may refer elsewhere. The X-ray peak profiles were also measured, and dislocation densities estimated, in a Bruker™ D8-Discover system with Lynxeye-XT™ linear detector. For details on dislocation density measurements, from X-ray peak profiles with momentum method, the reader may refer elsewhere[62] and also in appendix.

2.2 Modelling Framework

The input to our texture simulations comprised of 1024 grains. The corresponding crystallographic orientations were obtained by discretizing the experimental X-ray texture using the MTEX software[56]. Deformation texture simulations were performed using a rate-independent binary-tree-based continuum crystal plasticity simulations[55]. In particular, this model considered rolling induced plastic deformation as superposition of plane strain compression and simple shear in the RD-ND (rolling and normal directions) plane[14]. The simple shear has been attributed to geometric effects associated with the material flow path plus friction between the rolls and the workpiece. This is expected to decay linearly, along the ND, from its maximum at the workpiece surface to zero at the centre. Following the velocity gradient equation experienced by particular material point(s) during rolling:

$$L_{ij}=\begin{bmatrix}1 & 0 & \gamma_f \\ 0 & 0 & 0 \\ 0 & 0 & -1\end{bmatrix}L_{11}, \tag{1}$$

where, γ_f quantifies the net geometric and frictional effect, γ_f is henceforth termed the frictional shear strain which varied along the ND direction. $\gamma_f \in \{0, \pm 0.05, \pm 0.10, \dots, \pm 2.00\}$ was varied during unidirectional rolling and reverse rolling. The best fit texture was subsequently determined from texture difference indices (ID_N)[63]. It is to be noted that the numerical value of ID_N provides the most rigorous, and quantitative, difference between experimental and simulated orientation distribution functions or ODFs.

$$ID_N = \frac{\int (f_1(g) - f_2(g))^2 dg}{\int (f_1(g)^2) dg}, \tag{2}$$

$f_1(g)$ and $f_2(g)$ represent the experimental and simulated ODFs respectively, and dg denotes an infinitesimal volume element in orientation space. In this study, the γ_f corresponding to the minimum texture difference indices (ID_N) was taken to be the friction-induced shear. These were established, for UDR and RR, by a parametric study of texture simulations. Further details of the modelling framework can be found in the appendix section.

3. Results from Experiment and Modelling:

3.1 Experimental Results

As pointed out in the earlier section (section 2.1.), this study used direct observations on surface grains before and after UDR and RR, see Figure 1c. Though macroscopic strains appeared identical between the two rolling processes, there were differences in the movement of material points (see Figure 1b). The latter appeared to bring in differences in mesoscopic local shear strains (see Figure 2) and misorientations (see Figure 3). Unfortunately, the former could not be precisely quantified with digital image correlation, as the speckle patterns were getting somewhat smudged. Hence, an alternate method was adopted. From the grain boundaries, and using a method proposed by Keskar et al.[64], near boundary mesoscopic shear strains (NBMS) were estimated and plotted, see Figure 2a. It needs to be noted, and as mentioned in earlier studies[64,65] that the NBMS values were both positive and negative, and they often acted in opposite directions across the grain boundaries. Our measurements also indicated, qualitatively, that the RR had more negative shear. However, exact magnitude of positive and negative shear strains were difficult to estimate accurately. What emerged from our measurements, with reasonable certainty, is shown in Figure 2b – RR had more NBMS than UDR (0.34 versus 0.26). Subsequently, a parametric study on plasticity modelling has been attempted to bring out the values of local or redundant shear strains imposed during UDR and RR. It is to be noted that differences in imposed local shear strains on the surfaces of UDR and RR were an important attribute for differences in the evolution of surface microstructures. This has been described in further details in the subsequent paragraphs.

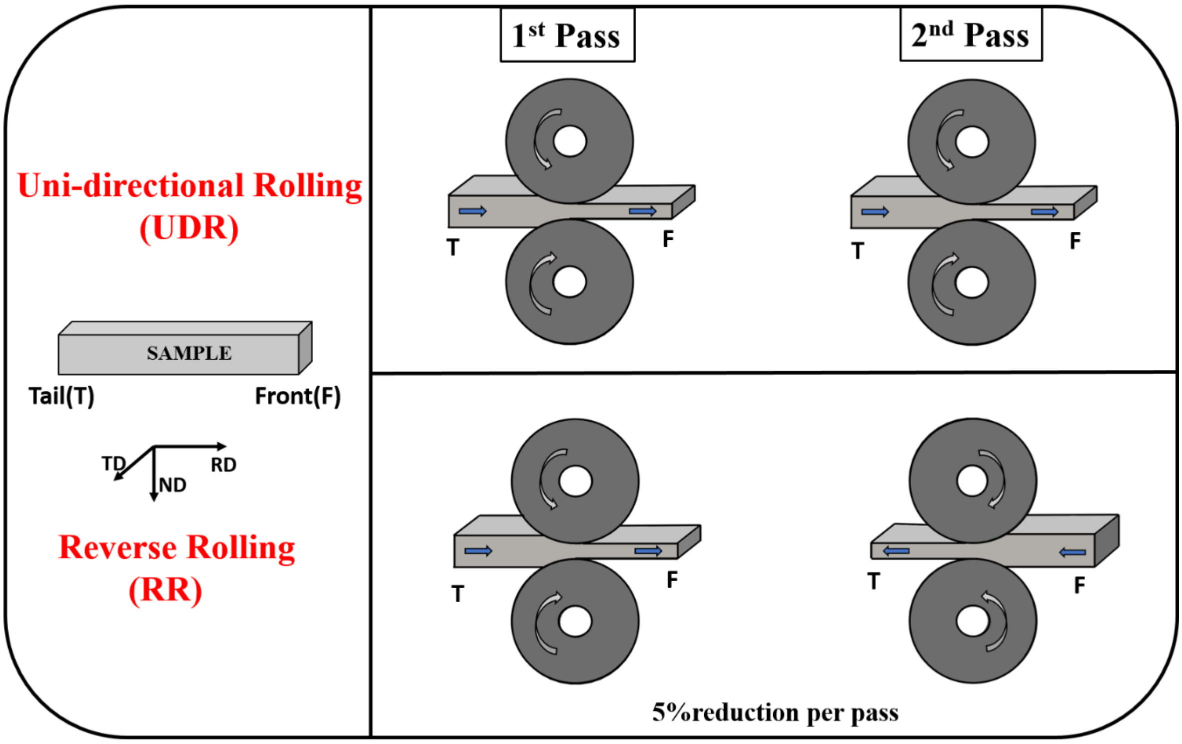

(a)

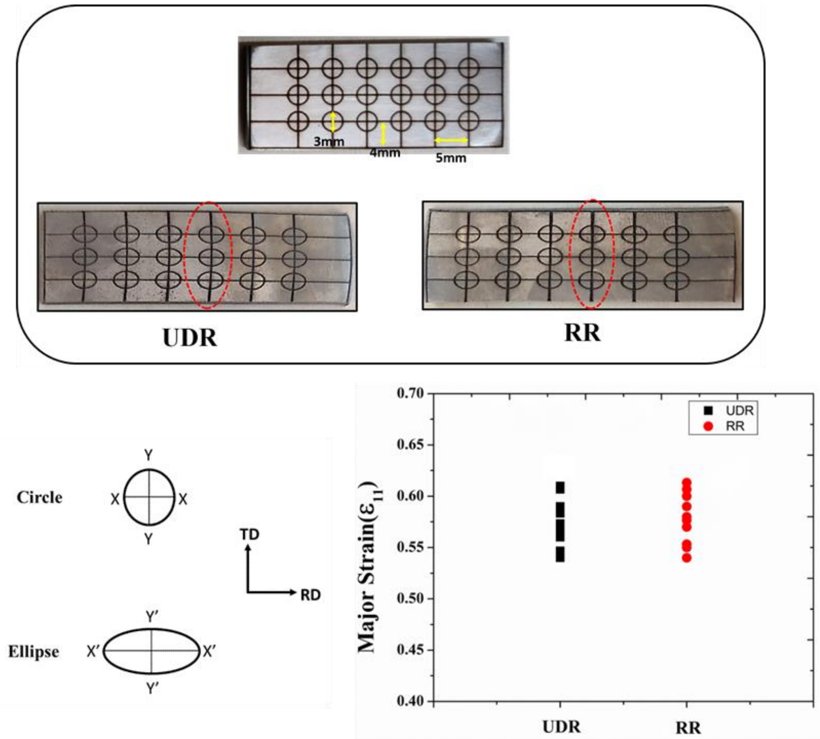
3mm
4mm
5mm
UDR
RR
Circle
Ellipse
TD
RD
Major Strain(ε_{11})
0.70
0.65
0.60
0.55
0.50
0.45
0.40
UDR
RR

(b)

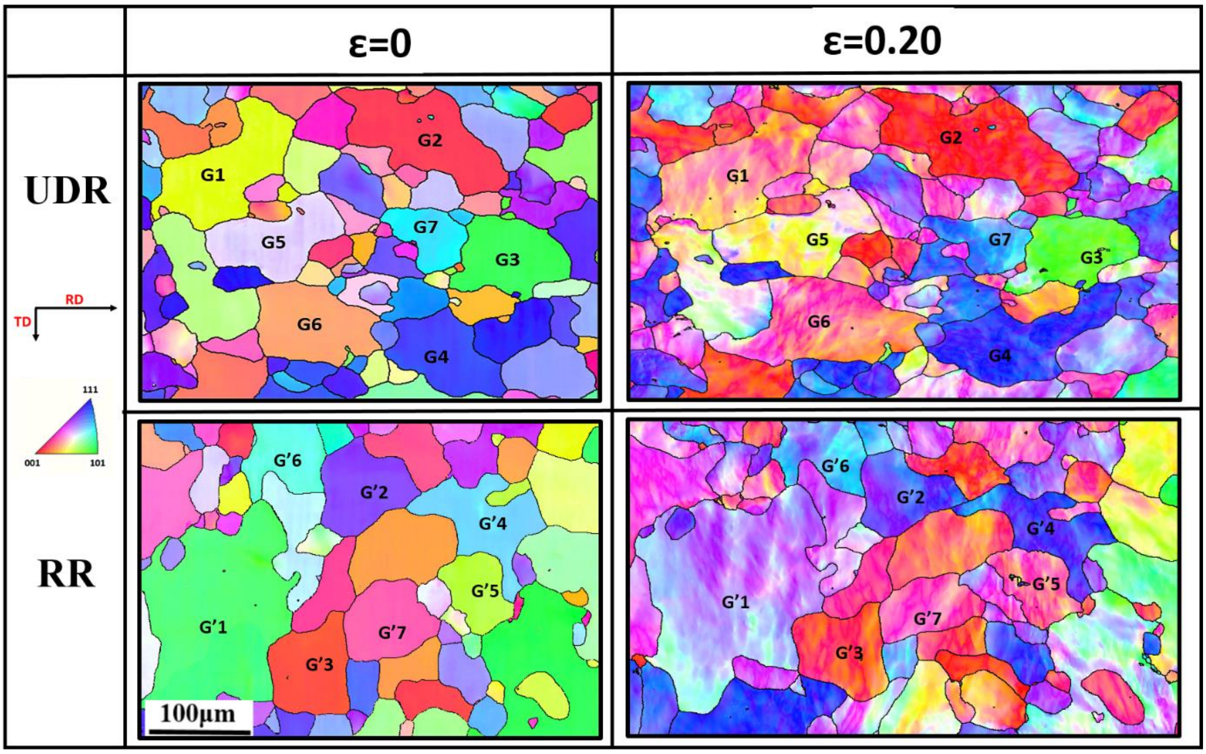

(c)

Figure 1:(a) Schematic of unidirectional rolling (UDR) and reverse rolling (RR). (b) Representative laser grids on the specimen surface and schematic for macroscopic strain measurements. Major strain estimates in UDR and RR. (c) Electron backscattered diffraction (EBSD) inverse pole Figure (IPF) maps from the same surface grains of IF steel before (ε = 0) and after (ε = 0.2) UDR and RR.

Table I. Chemical compositions (in wt% alloying elements) of the two steel grades used in this study.

ID	C	N	Mn	S	P	Si	Ni	Cr	Fe
IF	0.002	0.0032	0.08	0.006	0.015	0.004	0.02	0.014	Bal.
HSLA	0.11	0.0052	1.4	0.009	0.021	0.23	0.72	0.033	Bal.

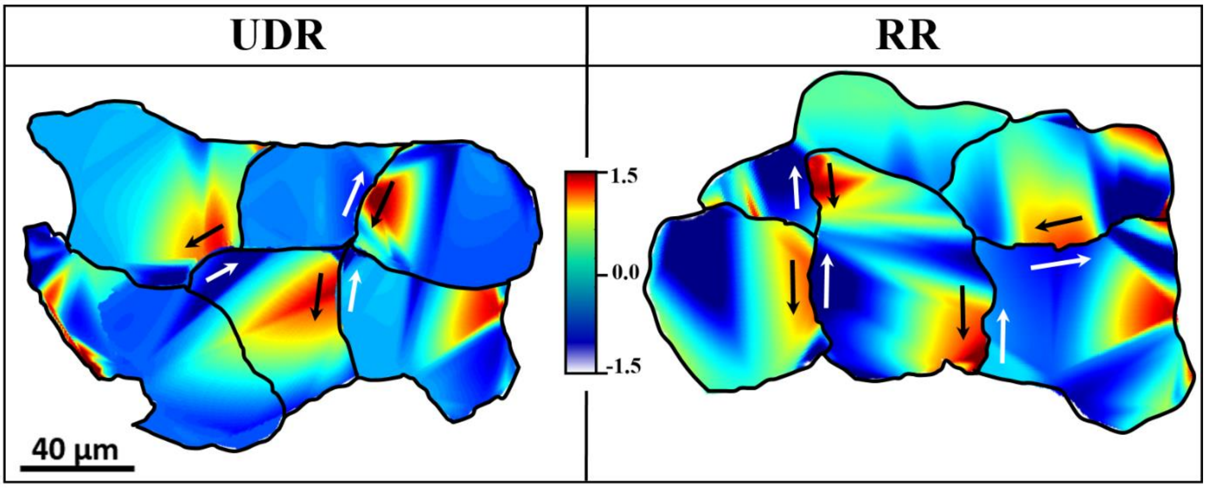

(a)

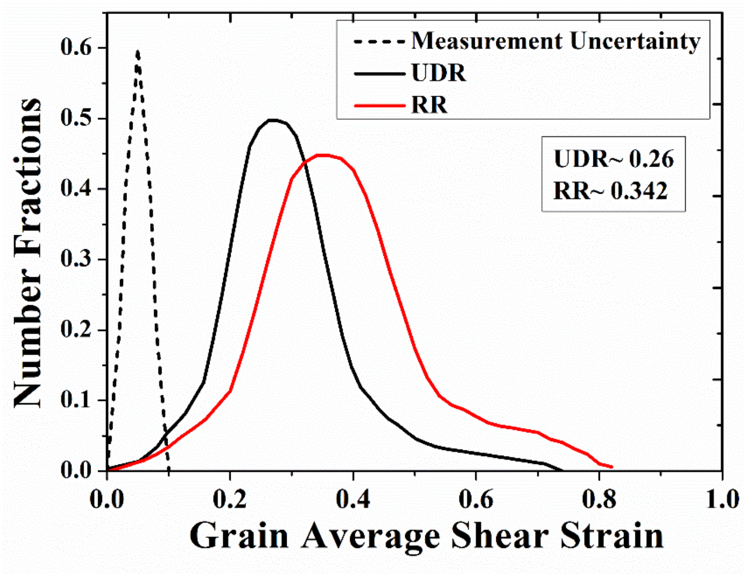

(b)

Figure 2: (a) In a grain cluster after UDR and RR (IF steel, for $\varepsilon = 0.2$), maps of near boundary mesoscopic shear (NBMS) strain[64]. (b) Distributions of average shear (NBMS) strain for UDR and RR. The estimated measurement uncertainty[64] is also included.

As shown in Figure 3, the surface microstructures of UDR and RR were noticeably different. This is shown as EBSD estimated maps of geometrically necessary dislocation (GND) density and grain reference orientation deviation (GROD), see Figure 3a. The GND densities were estimated from local Nye tensor plus optimized step size, and a method described elsewhere[66]. Further, a grain was identified by the continuous presence of a boundary > 5° misorienation and average (quaternion average) of each grain orientation was then estimated. The GROD represented misorientations of each measurement point in a grain from the grain average orientation. Data on GND density (Figure 3b) and GROD (Figure 3c) were estimated from ~200 surface grains, in both IF and HSLA, subjected $\varepsilon = 0.2$ PSC under UDR and RR. It is clear from Figure 3 that GND density and GROD were more in IF after RR (than UDR). However, the estimated difference between UDR and RR reduced significantly in the HSLA grade. It thus appears that the local or redundant shear (RR versus UDR) plus solute content (IF versus HSLA) determined the deformed microstructure evolution of the surface grains.

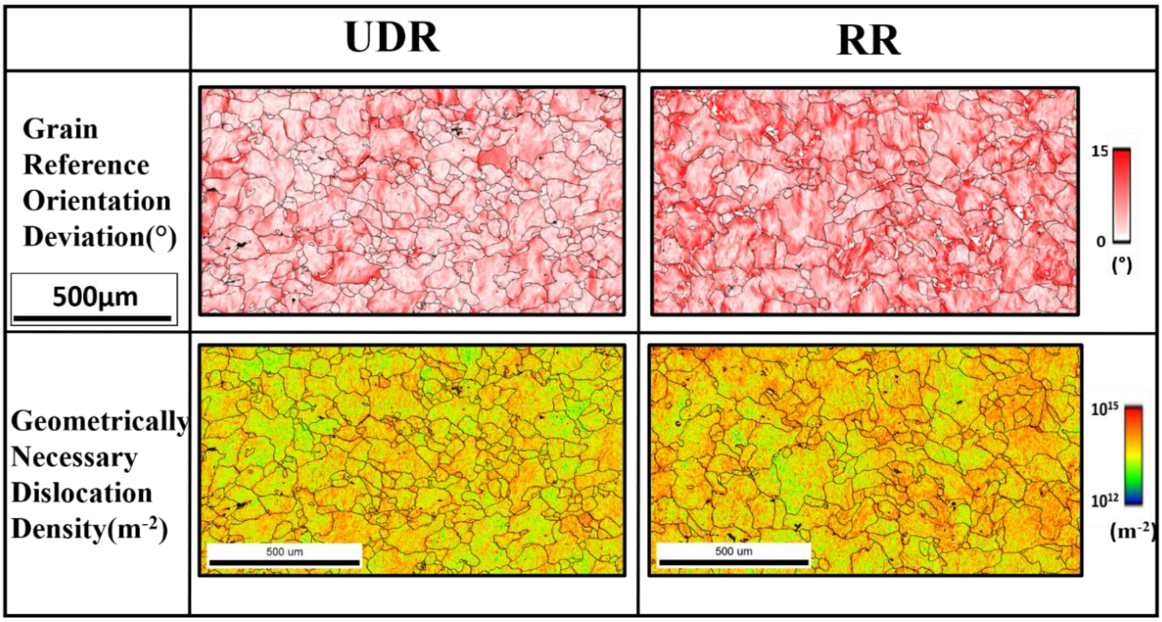

(a)

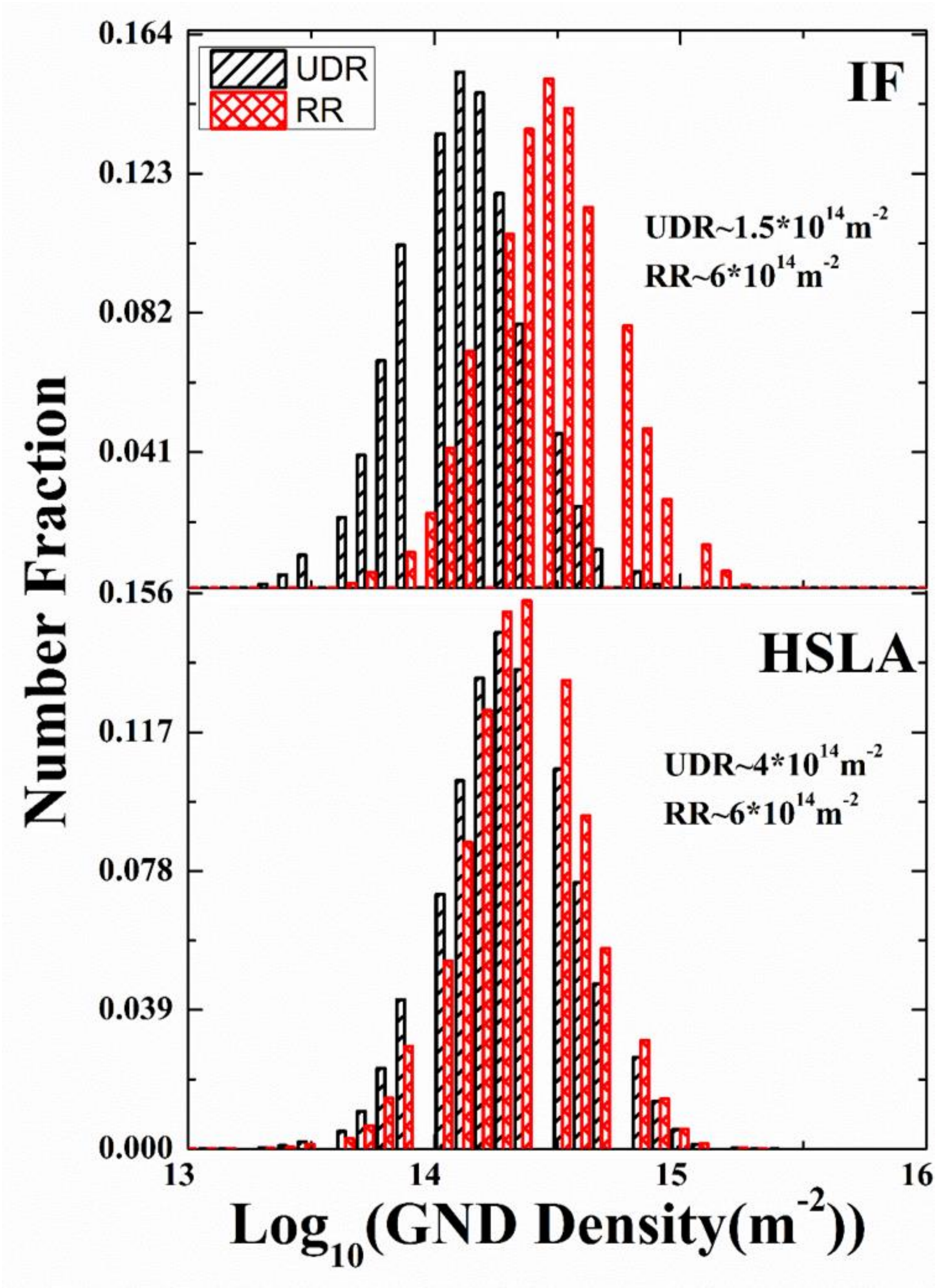

0.164
0.123
0.082
0.041
0.156
0.117
0.078
0.039
0.000
UDR
RR
IF
UDR~1.5*10^14 m^-2
RR~6*10^14 m^-2
HSLA
UDR~4*10^14 m^-2
RR~6*10^14 m^-2
Number Fraction
13
14
15
16
Log10(GND Density(m^-2))

(b)

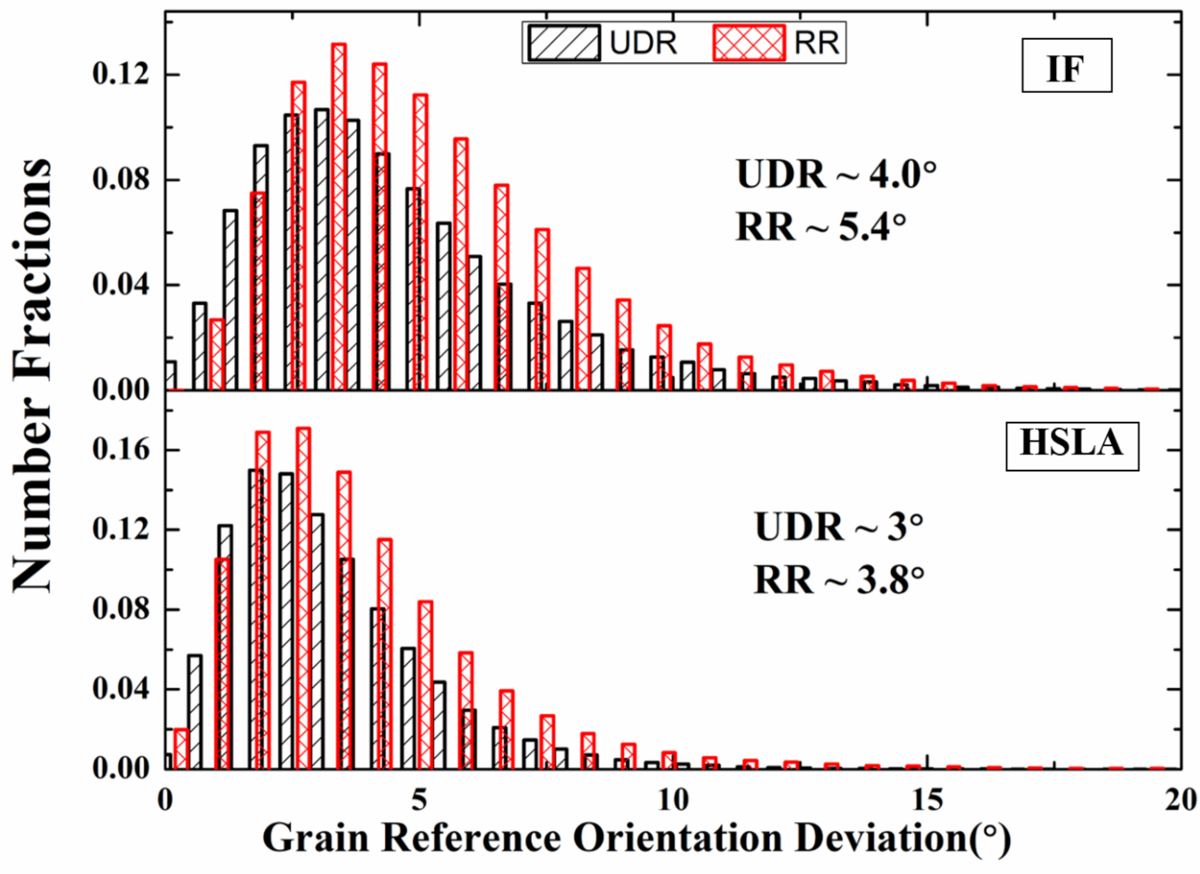

(c)

Figure 3:(a) EBSD estimated maps of grain reference orientation deviation (GROD) and geometrically necessary dislocation (GND) density. These are shown for IF steel, at $\varepsilon = 0.2$, subjected to UDR and RR. (b) GND and (c) GROD distributions for both IF and HSLA subjected to UDR and RR at $\varepsilon = 0.2$.

The crystallographic textures of steel, in particular low carbon steels, are often generalized as ND//<111> or γ-fibre and RD//<110> or α-fibre[2,42,67–70].These fibres, and associated ideal orientations (both bcc rolling as well as shear texture components[71]), are shown in a $\phi_2 = 45^o$ section of orientation distribution function (ODF) in Figure 4a. It is to be noted that we have used triclinic (and not orthorhombic) symmetry. This (ϕ_1 ranging from 0-360^o) was necessary to capture the shear texture. It has been reported[72–74], especially in IF steel, that post rolling γ-fibre has more misorienation and dislocation density than the α-fibre. In particular, orientation dependent appearance of grain interior strain localizations in rolled γ-fibre grains are known to provide higher stored energy of cold work[67,68,72–77] in low carbon steel. This is critical, as it controls the formation of recrystallized texture, vital for the formability of low carbon steel[67,68,75,77,78]. Direct observations (Figure 4b) of IF surface grains showed, qualitatively, that grain interior strain localizations were more in γ-fibre grains after UDR but not after RR. Figures 4c and 4d plot the difference between fibres and ideal orientations as distributions of GND densities, and the earlier microstructural representation (Figure 4b) has been made quantitative. In summary, orientation dependent stored energy of cold work was observed only in the surface grains of low solute IF undergoing UDR. This was largely absent in IF subjected to RR, and was not observed (though results are not shown for brevity) in high solute HSLA.

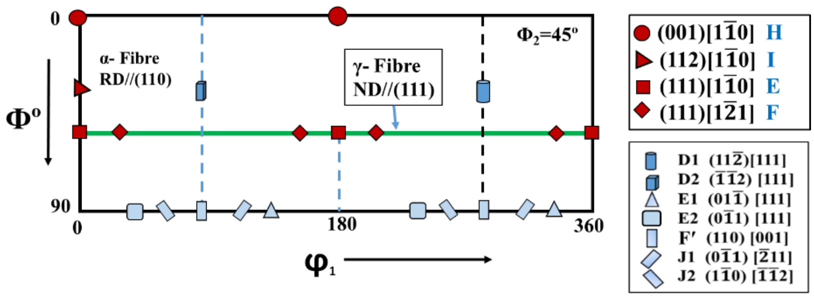

(a)

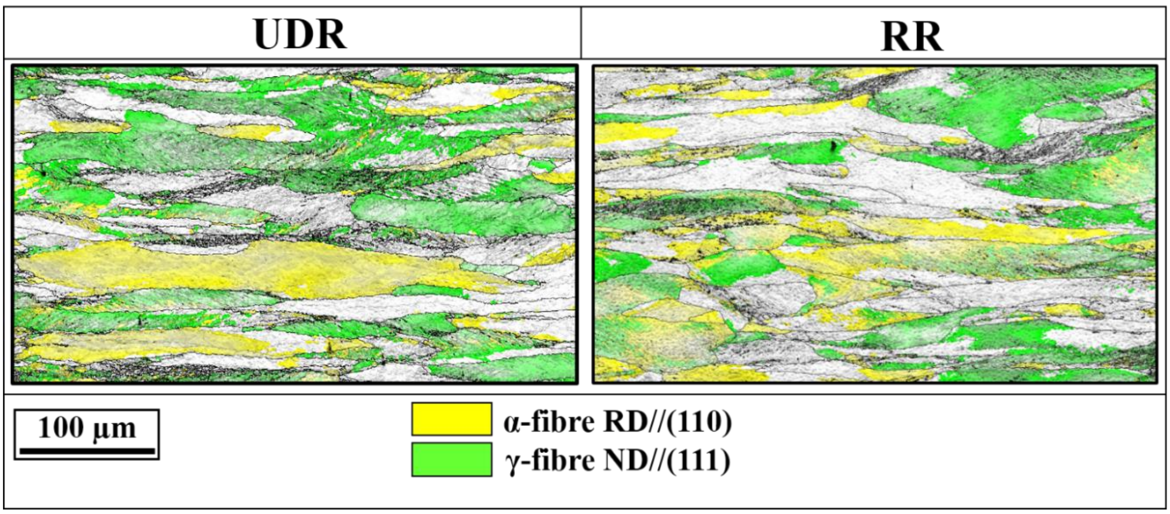

(b)

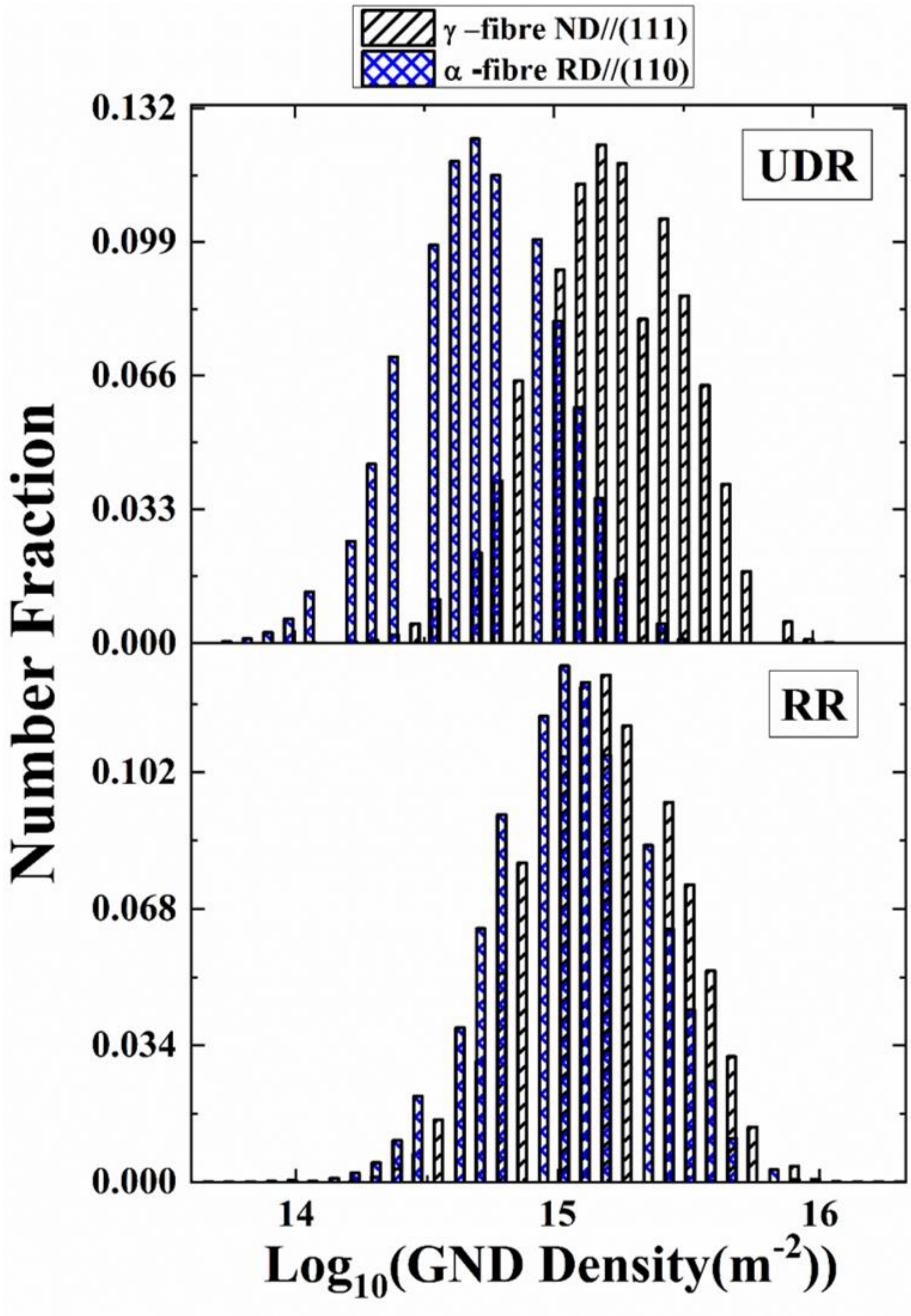
γ –fibre ND//(111)
α -fibre RD//(110)
UDR
RR
Number Fraction
0.132
0.099
0.066
0.033
0.000
0.102
0.068
0.034
0.000
14
15
16
Log10(GND Density(m-2))

(c)

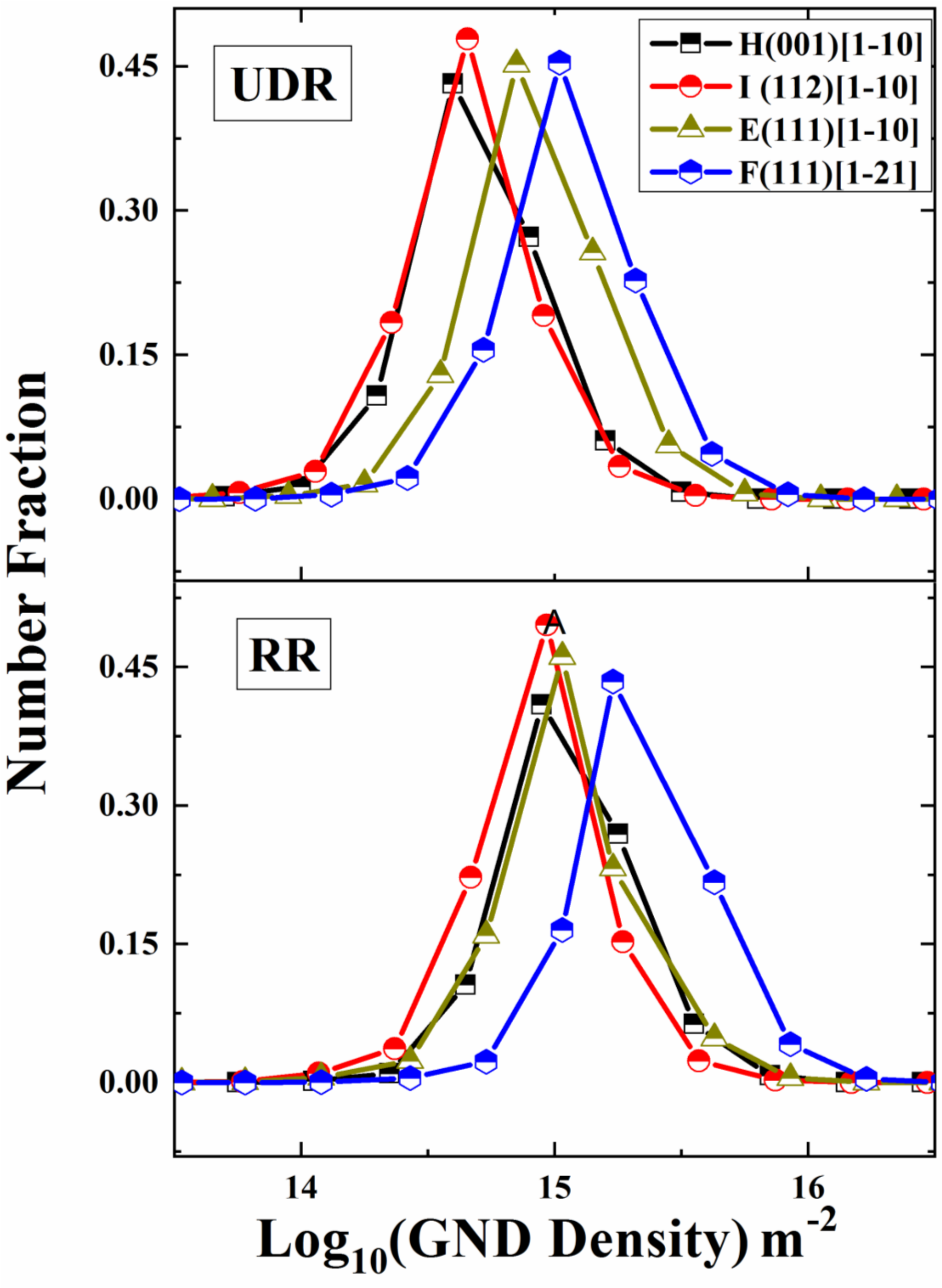

(d)

Figure 4: (a) Standard ϕ_2 = 45° orientation distribution function (ODF) section showing ideal bcc texture fibres and orientation[2] along with shear texture components[71]. (b) Surface grains, γ-fibre (ND//<111>) and α-fibre (RD//<110>), of IF subjected to UDR and RR at ε = 0.6. GND density distributions for (c) γ and α fibres and (d) their components or ideal orientations. These are also shown for IF surface grains subjected to UDR and RR at ε = 0.6.

Further confirmation of orientation-dependent microstructure evolution was obtained by X-ray diffraction or XRD, see Figure 5. This involved dislocation density measurements with XRD peak profile[79] analysis (Figure 5a) and d-sin$^2\psi$ measurements[60] of residual strain. For ease of comparison, Figure 5a shows normalized (with respect to fully recrystallized state) dislocation density estimates, while residual strains (Figure 5b) estimates are expected[80] to represent both GND density and dislocation configurations. Further, the X-ray estimated dislocation densities have been compared with EBSD estimated GND densities, and are shown in supplementary Figure S1. Figure 5 thus reiterates, albeit with higher statistics but limited orientation information, the points emerging out earlier from Figure 4. IF subjected to UDR had highest difference between the X-ray poles or plane normals. This difference diminished, noticeable for IF subjected to RR, and was largely absent in HSLA.

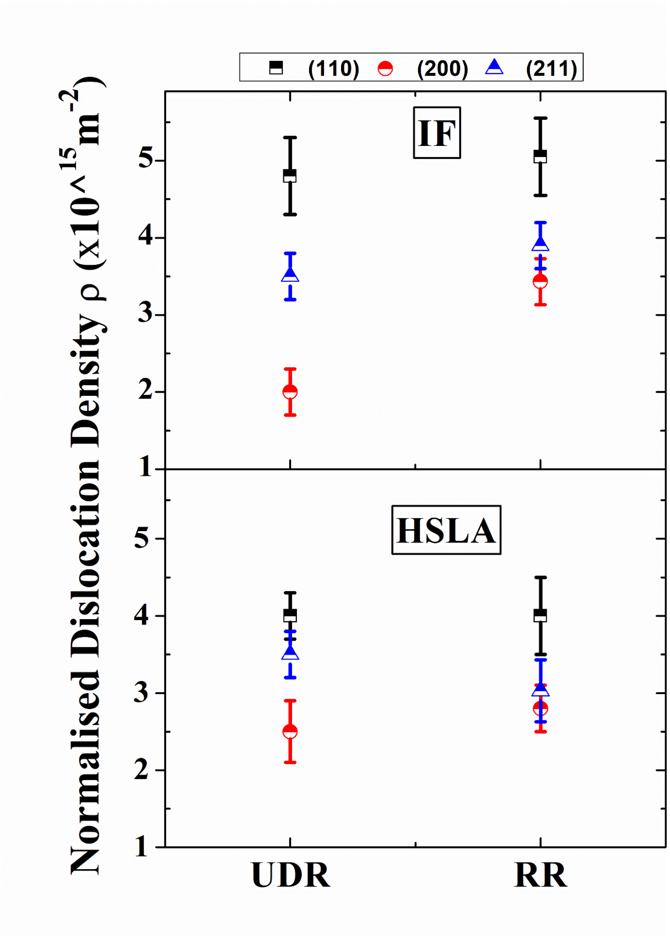

(a)

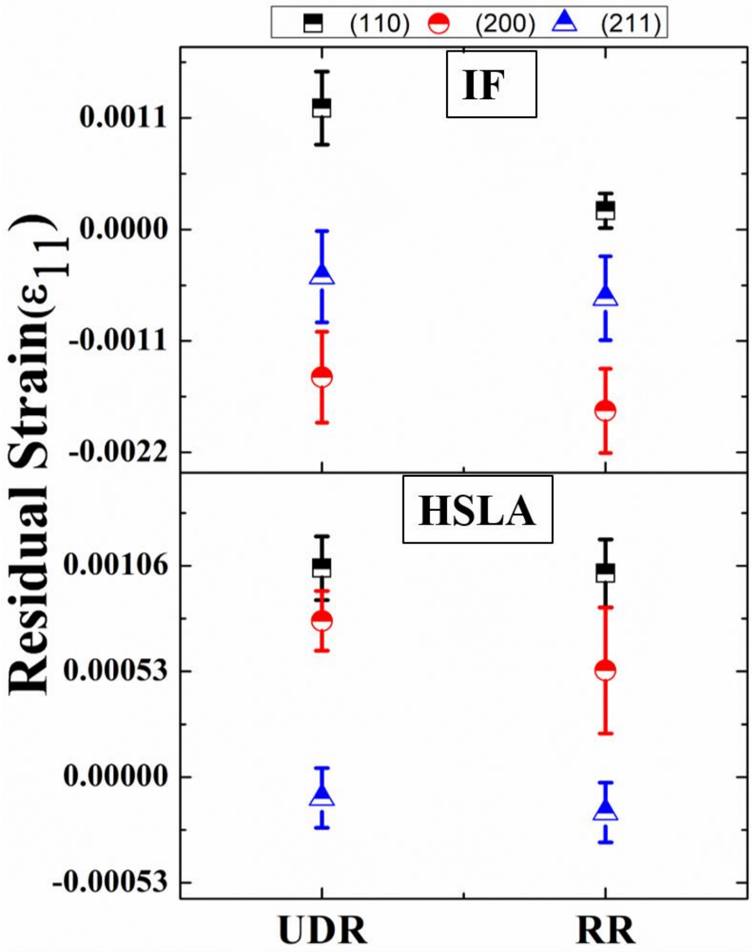

(b)

Figure 5: XRD estimated (a) normalized dislocation density and (b) residual strain ε_{11} (residual strain on the rolling plane and along rolling direction). These are shown, for different poles or plane normals, in for both IF and HSLA surface grains subjected to UDR and RR at ε = 0.6. In (a), the dislocations densities (normalized by values measured at ε = 0) were estimated from peak profile analysis[62], while in (b) residual strains were measured by standard d-$\sin^2\psi$ method[60].

As both EBSD and XRD measurements indicated a rolling mode (UDR or RR) dependent substructure formation in the IF surface grains, these were investigated further with transmission kikuchi diffraction (TKD) and transmission electron microscopy (TEM) – see Figure 6. In particular, the dislocations were present as dislocation boundaries and as cell interior dislocations. The former may be classified[2,81] as dense dislocation walls (DDWs) and microbands (MBs), while the latter may be generalized as statistically stored dislocations

(SSDs) – ranging from random dislocation arrays (Taylor lattices) to relatively well formed substructures. As shown in Figure 6a, dislocation boundaries were more after RR while UDR had more SSDs. In particular, the MBs and DDWs were mostly non-crystallographic or first generation[52,81–83], as their traces often did not fall within 5º of closed packed planes (Figures 6b and 6c). Figures 6b and 6c collate observations from the rolling plane, while Figure 6d does the same for the long transverse (RD-ND) section. UDR showed, in general, more random dislocation arrays and less well formed DDWs and MBs even in the RD-ND section. Further, there were clear differences between γ-fibre (ND/<111>) and non γ-fibre substructures (see Figure 6d) in the UDR specimen. Additionally, γ-fibre subjected to UDR clearly revealed more aligned MBs and DDWs. This was not the case for the RR. In summary, orientation dependent substructure formation in the UDR of IF was clearly reflected in the difference in substructures, and higher densities of first generation or non-crystallographic DDWs and MBs.

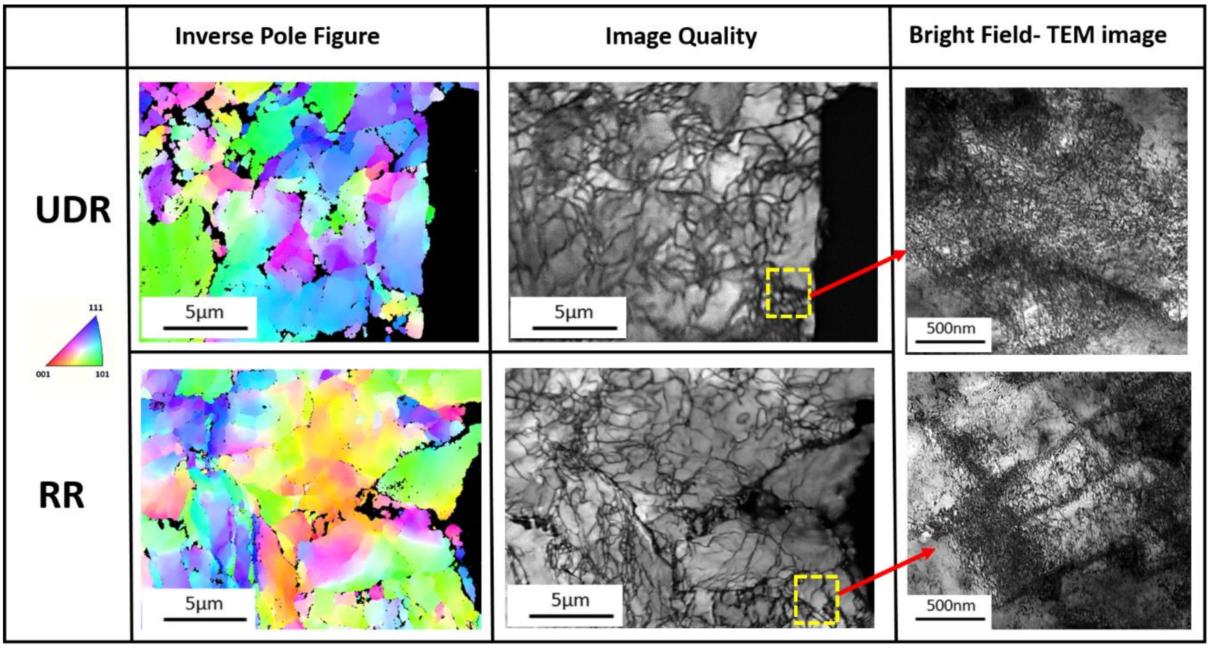

(a)

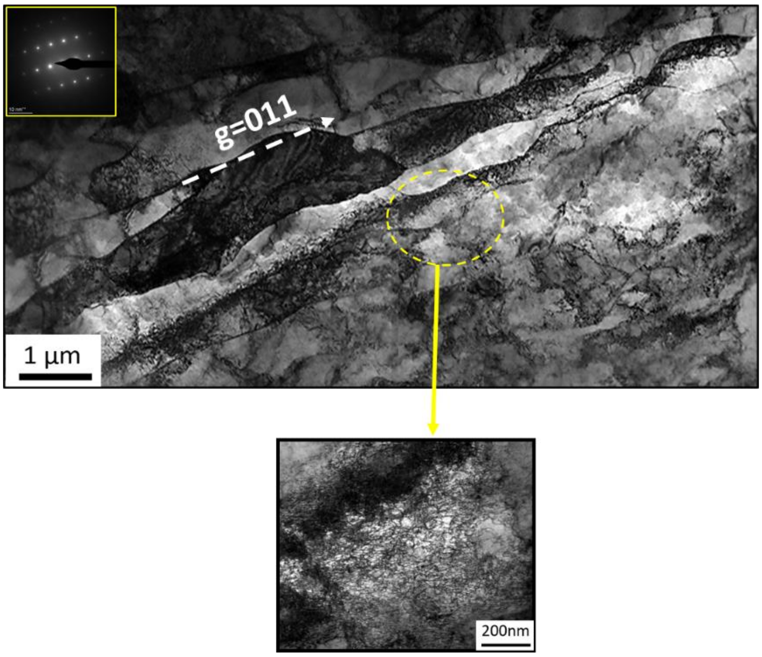

(b)

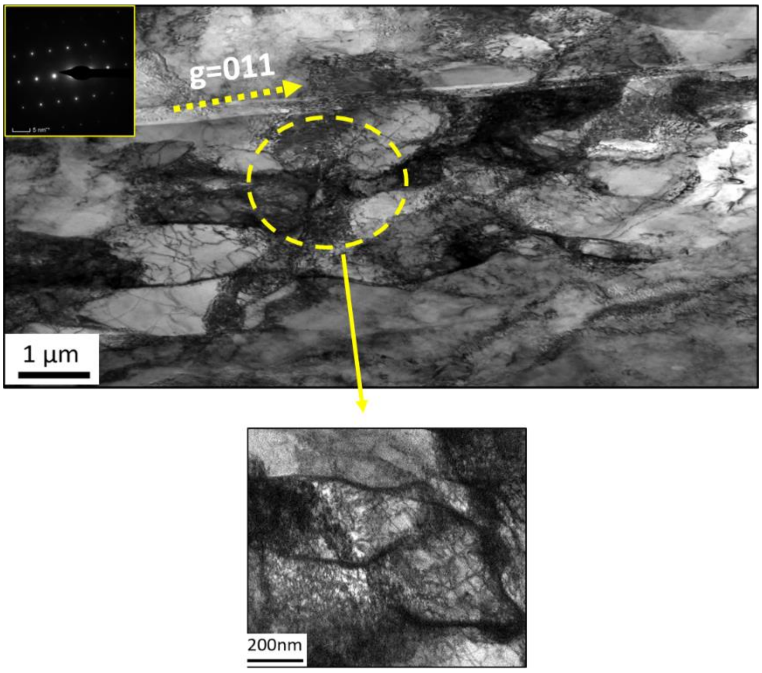

(c)

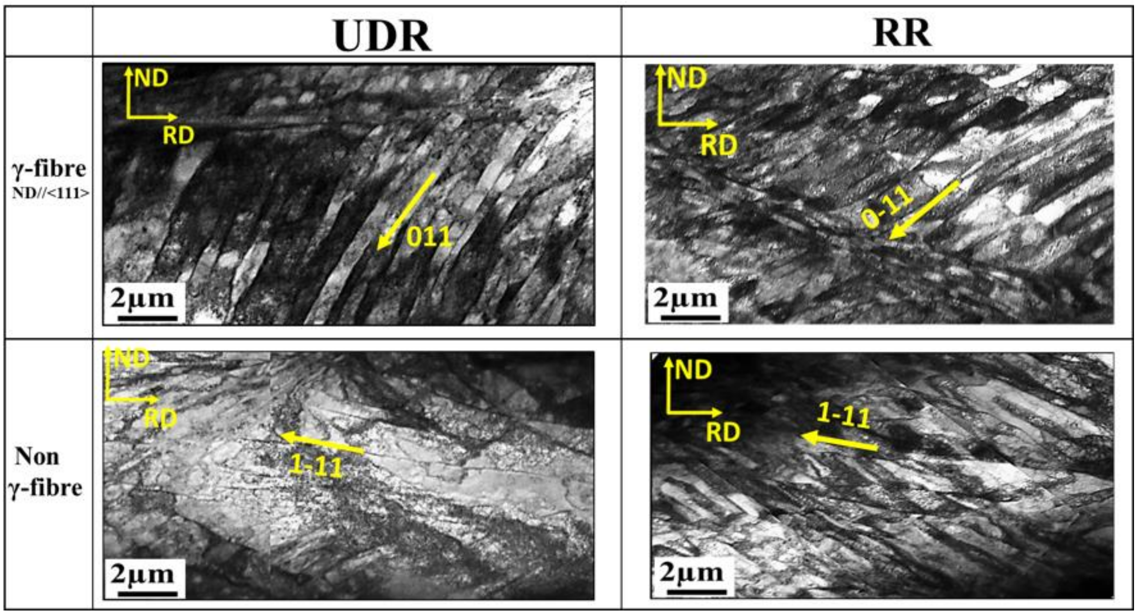

(d)

Figure 6: (a) Combination of transmission kikuchi diffraction (TKD) and transmission electron microscopy (TEM) were used to bring out differences in substructure developments in IF surface grains after UDR and RR (at ε = 0.6). TEM characterization of the substructures on RD-TD plane in (b) UDR (c) RR surface grains and on (d) RD-ND (long transverse section) plane in UDR and RR.

This study also measured bulk crystallographic textures for surfaces (T0), see Figure 7. Irrespective of the grade, IF (Figure 7a) and HSLA (Figure 7b), the surface textures differed noticeably between UDR and RR. However, and as shown with sub-surface ODF sections later in this manuscript (section 3.2.), the mid-thickness textures were identical. Differences in the T0 textures can be further expanded in terms of rolling and shear texture components (figure 4a). These (respective volume fractions of γ-fibre and shear components) are indicated in Table II. Ideal ND//<111>, for example, was higher in IF but did not differ noticeably with the rolling route (UDR and RR). In contrast, the total shear components were similar between the grades, but appeared higher for RR. The texture differences were further substantiated from the texture estimated r-bar values at different angles to the rolling direction, see Van Houtte[57]. As shown in Figure 7c, these (between UDR and RR) were identical at T/2 (mid-thickness) but differed significantly at T0 (surface). This was true for both grades. In brief, UDR versus RR showed noticeable quantitative difference in surface (T0) crystallographic textures, irrespective of the grade. Our continuum plasticity modelling plus texture simulations were then adopted to bring out the rationale behind such differences.

Table II: Volume fraction of ND//<111> and combined shear texture components as obtained from ODFs using MTEX^{TM}[56] with a tolerance angle of 10º.

Texture component	HSLA		IF	
	UDR	RR	UDR	RR
ND//<111>	0.23	0.25	0.28	0.29
Shear Components	0.275	0.284	0.254	0.282

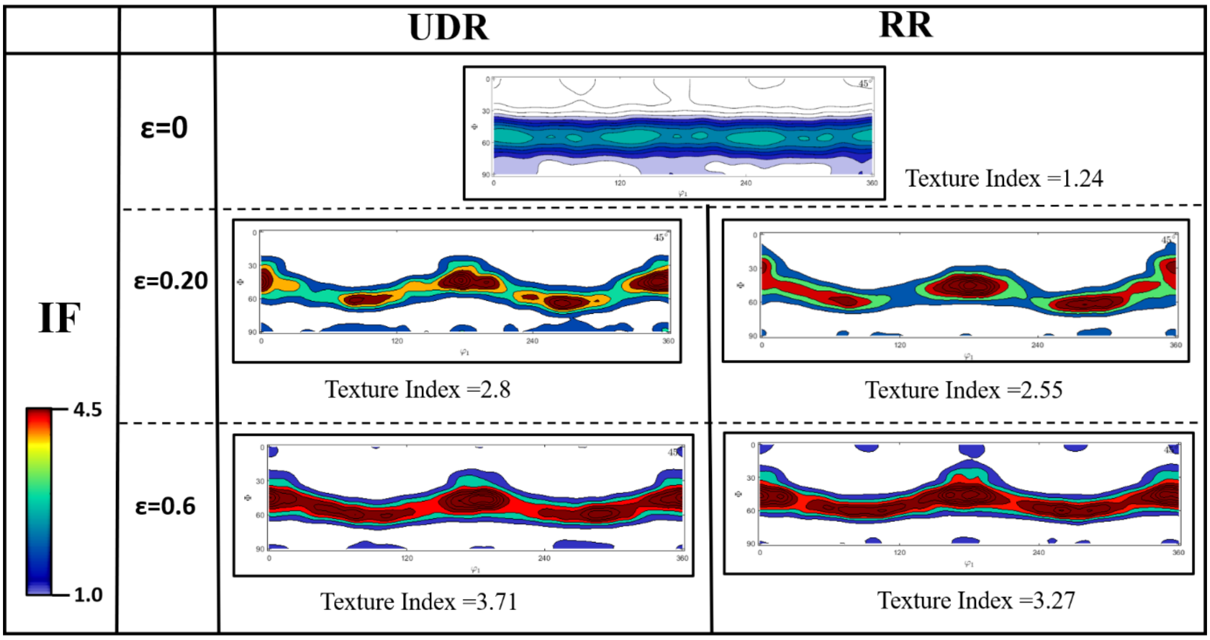

(a)

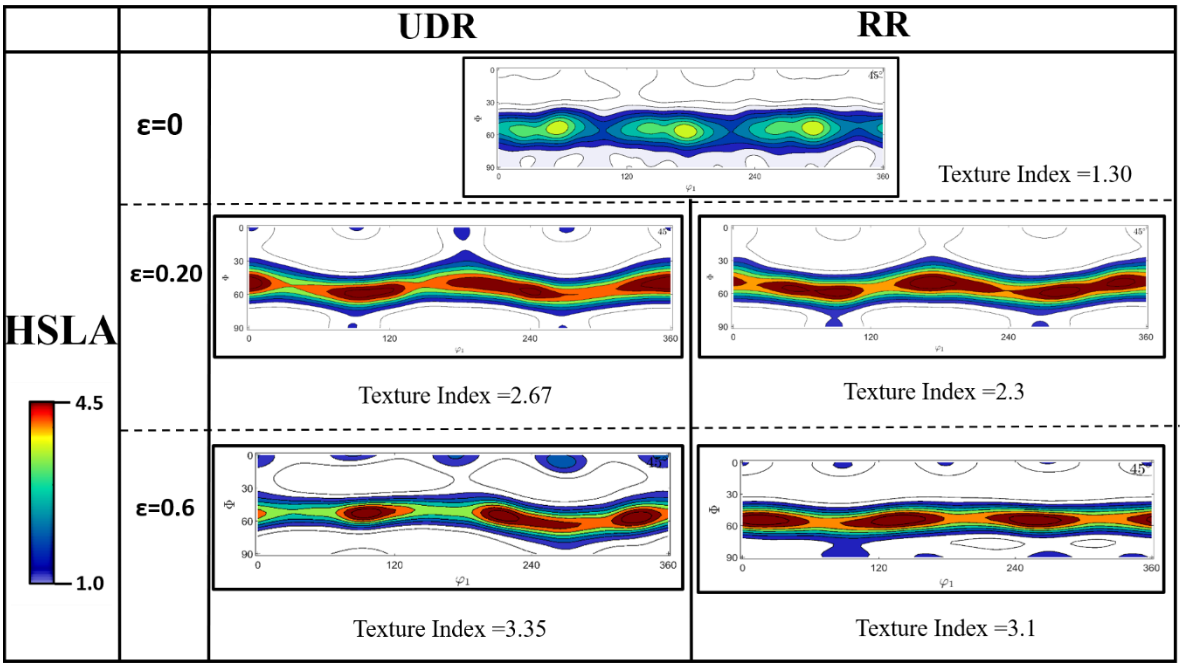
UDR
RR
HSLA
ε=0
ε=0.20
ε=0.6
4.5
1.0
Texture Index =1.30
Texture Index =2.67
Texture Index =2.3
Texture Index =3.35
Texture Index =3.1

(b)

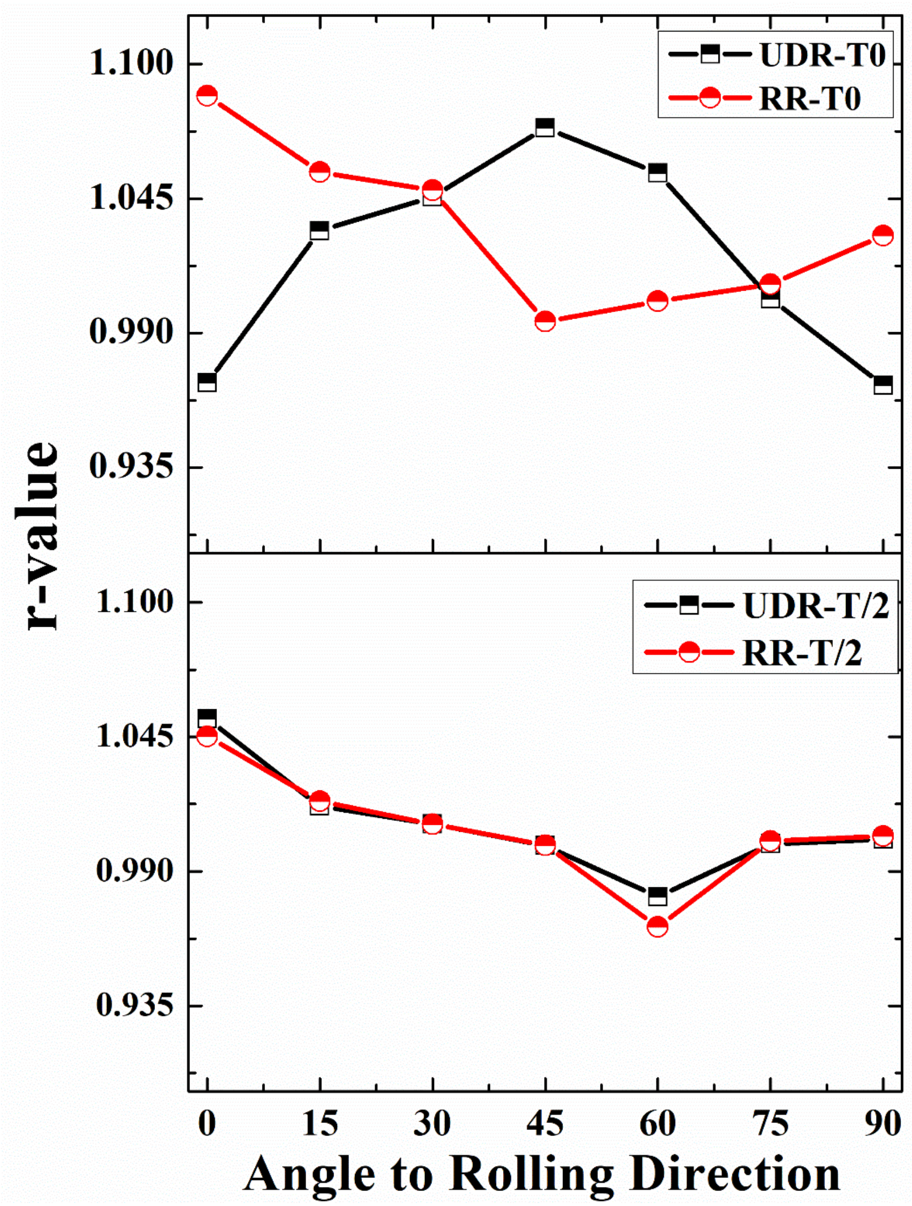

(c)

Figure 7: ϕ_2 = 45° ODF sections showing bulk crystallographic textures of the surfaces in (a) IF and (b) HSLA, subjected to UDR and RR at ε = 0, 0.2 and 0.6. (c) R-values[57], at different angles to rolling direction, at surface (T0) and mid-thickness (T/2) of ε=0.6 rolled (UDR and RR) IF steel.

3.2 Results from Crystal Plasticity Modelling and Texture Simulations:

We have used a binary-tree based texture modelling, described earlier in section 2.2 and in the appendix. As shown in Figure 8a, the model used an idealized microstructure under a balanced binary tree-based representation[55]. Further, the role of surface shear (γ_f) on different 'layers' of the rolled material were considered, see Figure 8b. Experimental textures, see Figure 8c, were identical and orthorhombic in nature at the T/2 section for both UDR and RR. Deviation from ideal orthorhombic texture[2,84], as expected from introduction of a shear component[14,15,18,41] , happened at T/4 and more so at T0. In brief, a clear texture gradient was experimentally observed.

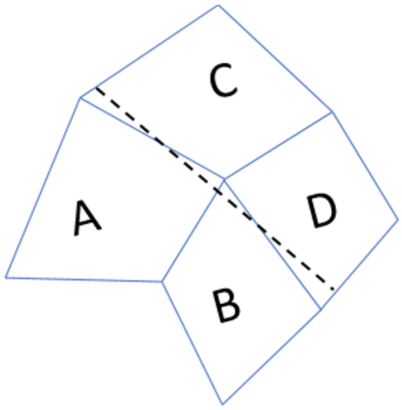

(i)

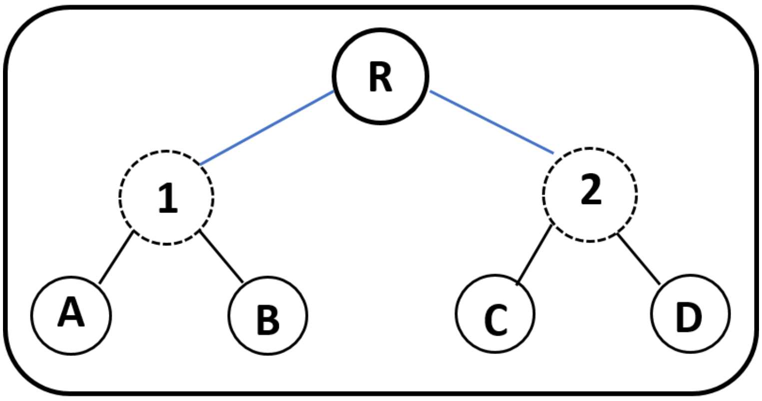

(ii)

(a)

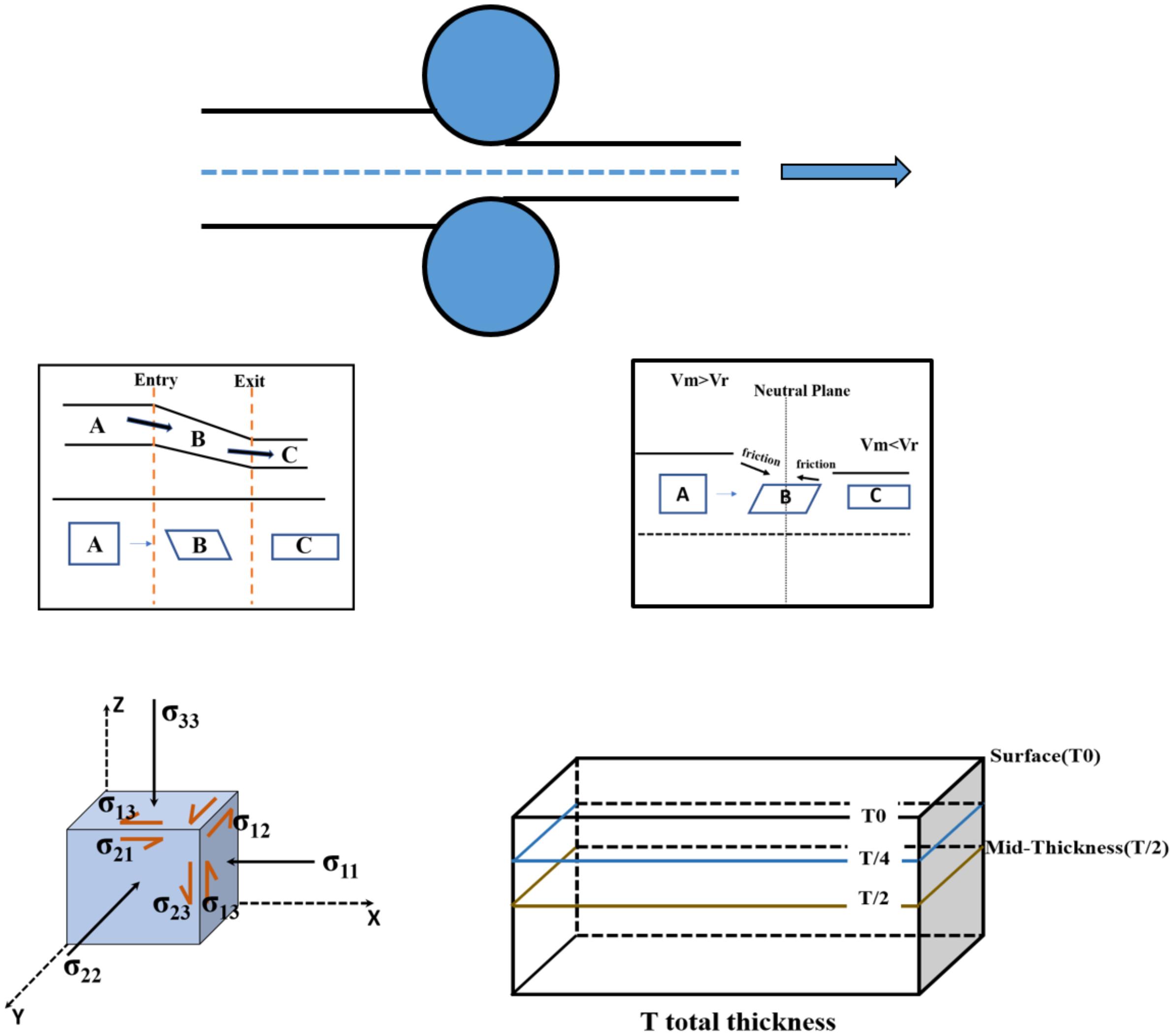
Entry
Exit
A
B
C
A
B
C
Vm>Vr
Neutral Plane
friction
friction
Vm<Vr
A
B
C
Z
σ_{33}
σ_{13}
σ_{12}
σ_{21}
σ_{11}
σ_{23}
σ_{13}
X
σ_{22}
Y
Surface(T0)
T0
T/4
Mid-Thickness(T/2)
T/2
T total thickness

(b)

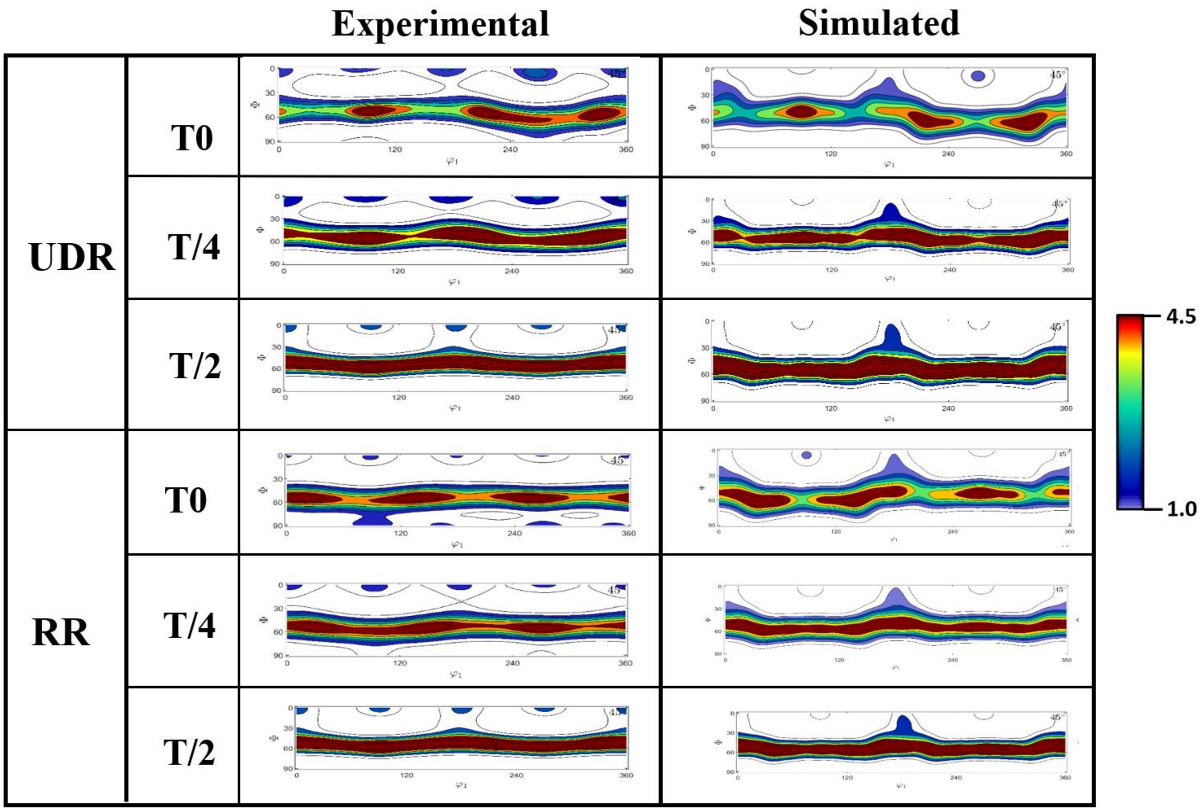

(c)

Figure 8:(a) Schematic of 4-grain microstructure in a binary tree-based model[55]. This included, (i) idealized microstructure and (ii) balanced binary tree-based representation. (b) Schematic of the effect of rolling geometry and friction direction on shear in rolled material and different layers taken for texture measurements and simulations. (c) Through thickness experimental and simulated textures, with ϕ_2 = 45° ODF sections. The simulations used the binary tree-based model.

Texture developments in the UDR and RR specimens were modelled by treating the plastic deformation as only PSC ($\gamma_f = 0$ in eq. 1) at T/2. This predicted a γ-fibre, see Figure 8c, texture nearly identical to that of the experimental one. This is not surprising, as binary-tree or ALAMEL models are known[43,55,85] to faithfully predict experimental rolling textures, especially by accounting for grain-to-grain interactions. In order to approach experimental textures at other 'layers', especially T0, it was found necessary to impose shear strains ($\gamma_f \neq 0$

in eq. 1), as detailed in section 2.2. A parametric study on imposed γ_f was conducted and best fitted textures are then collated in Figure 8c.

The difference between experimental and simulated textures has been best captured by texture difference indices ID_N[63]. As shown in Figure 9a, considering pure PSC ($\gamma_f = 0$ in Eq. 1) this was negligible for T/2, but increased for T/4 and more so for T0. It is thus clear, albeit indirectly, that imposed strain mode differed at T/4 and especially at T0 sections from ideal PSC. A parametric study on imposed γ_f was then conducted for the surface textures, see Figure 9b. It is clear that texture difference indices ID_N was lowest for γ_f^* = +1.25 and γ_f^{**}= -0.85, for UDR and RR T0 textures, respectively. Further, textures were considered to vary linear from T0 to T/2, and best fitted textures for different UDR and RR cross-sections (example: T/4) were obtained. These, listed in Figure 8c, captured the experimental breakup of γ-fibre with imposed shear extremely well. In brief, the difference in texture developments between UDR and RR were clearly attributed to quantifiable differences in local or redundant shear, and were modelled very successfully.

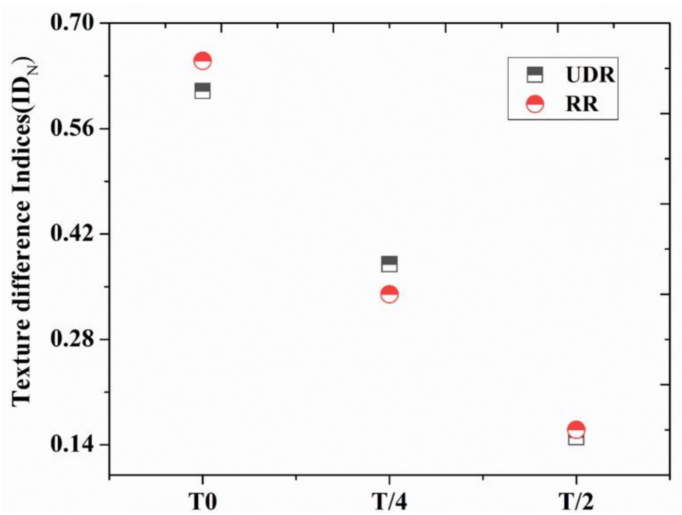

(a)

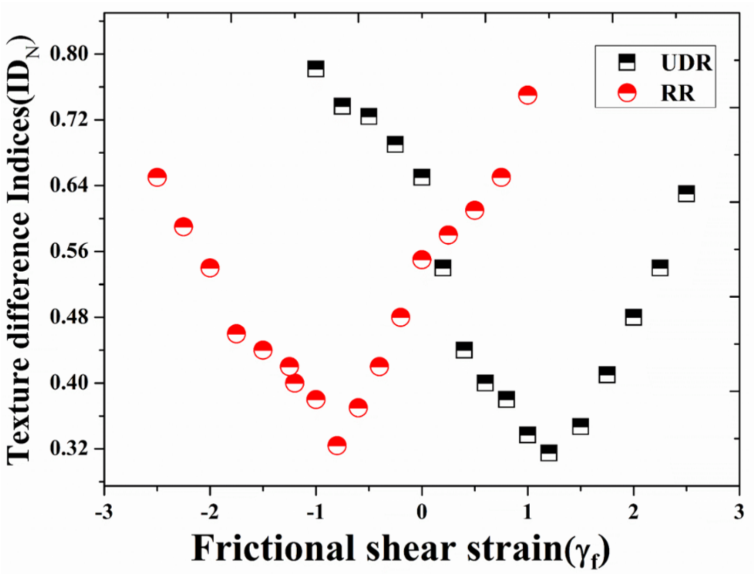

(b)

Figure 9: Texture difference indices ID_N (eq.3)[63] variation for (a) different through-thickness locations with zero local shear ($\gamma_f = 0$) and (b) parametric study of different values of γ_f at T0 section. These are presented for HSLA subjected to UDR and RR and $\varepsilon = 0.6$.

4. Discussion:

Important attributes of rolling texture developments are formation of deformation fibres plus texture components, and the presence of an orthorhombic symmetry[42,68,69,78]. Any deviation from the latter is due to the introduction of 'redundant shear' in the PSC strain matrix[12–14,16,18] Introduction of this shear, especially with asymmetric rolling and accumulative roll bonding, has also been related to different substructure evolution and grain fragmentation[2,18,25,33,86,87]. Though there exists an extensive array of literature on the overall subject, rarely the exact role of local or redundant shear on the as-rolled microstructure and crystallographic texture has been systematically explored with a comprehensive but simplistic approach. This has been the niche of the present study.

Truszkowski et al.[12,13] attributed the through-thickness inhomogeneity in rolling texture to the frictional shear and non-uniformity in the penetration of this shear strain. Region of draught during plain strain rolling deformation seemed to be crucial as far as development of shear was concerned. However, this excellent approach[19] appears somewhat incomplete by a qualitative explanation on texture rotations and a corresponding qualitative transition from rolling to shear texture. It would have been ideal to approach this problem with quantitative texture simulations. However, attempts have also been made to model the development of through thickness texture gradient by incorporating the shear strain component under appropriate texture simulations[14,16,17,40,45,47]. Over the years, the texture simulations have evolved – from the full constraint Taylor to relaxed constraint and visco-plastic self-consistent framework and more recent ALAMEL and binary-tree approach[55,63,70,85,88–92].

The original Taylor simulations overpredicted the developments in rolling textures[89]. This has been attributed to the Taylor's assumption of iso-stress, and hence neglecting the interactions between the neighboring grains. This was partly resolved in relaxed constraint Taylor and in rate sensitive models. However, all Taylor type simulations need to balance between the local relaxation of strain, while minimizing back-stresses. The latter is essential for introducing shear components[63]. Of course, this problem can be addressed by computationally expensive full-field crystal plasticity finite element modelling (CPFEM),[70] especially by incorporating strain gradients. However, a more elegant, and computationally inexpensive, route is through an appropriate pairing of grains in a continuum framework[55,88]. This has been the origin of continuum models like ALAMEL and binary-tree, which has been, arguably, as effective as CPFEM[63] in approximating near grain boundary strain(s) and orientation gradients and hence for quantitative deformation texture simulations[43,63]. Such models are extremely effective in capturing deformation texture evolution independent of the strain mode, and are 'at per' with computationally intensive full-field crystal plasticity finite element[93].The present study adopted the approach of binary-tree based continuum modelling. Further, our texture simulations (see Table S1 in supplementary material) were effective in capturing minor shear texture components very effectively.

It was important to approximate differences in through-thickness strain gradients in a simplistic yet effective way. For this a simple analytical approach of location dependent strain field, as proposed originally by Lee and Duggan[14], was adopted. As described in the earlier sections, the surface shear strains were approximated as positive and negative γ_f, respectively, for the processes of UDR and RR. Parametric binary-tree texture simulations (Figure 9b) then approximated the values of local shear strain (γ_f), bringing out the defining role of strain mode plus local or redundant shear on the developments of crystallographic textures in bcc steel. The reversal of shear strain tensor clearly brought out the surface inhomogeneity in textural development in both the rolling modes.

Earlier studies were expressing the effectiveness of deformation texture simulations by qualitative comparison of pole figures, ODFs and fibre intensities. These, however, can be extremely misleading[2,92], as the texture intensities depend on the symmetry of a crystallographic orientation and hence its location in the Euler space. Even volume fraction estimates would suffer from such constraints. There are two possibilities of quantitative comparison between experimental and simulated textures. Firstly, a texture-estimated quantity such as r-values (normal anisotropy) can be compared, and effectiveness of a model brought out[43]. More rigorous method is, however, to provide a scalar differential between experimental and simulated ODFs – using the so-called texture difference indices (ID_N)[63] or eq. (2). It is to be noted that the numerical values of ID_N does not compare individual components, but provides the arithmetic differences between all points in the ODF space. We have used the ID_N to establish the role γ_f or the frictional shear component in predicting overall textures most effectively or quantitatively.

Further, the steels texture developments appeared dependent on the strain mode and shear; but independent of the solute content (example, IF versus HSLA). This was not the case for deformed microstructure evolution – a topic deliberated in the next paragraph. These results on deformation textures are clear and definitive, and can easily be translated (though that remains beyond the scope of the present study) to texture developments in asymmetric rolling or accumulative roll bonding.

An equally critical observation, though valid primarily on low solute IF, was the evolution of deformed microstructures, see Figures 3-6. In particular, more GNDs and misorientations were observed on the surface grains of RR (Figure 3), but they also had insignificant orientation sensitivity (Figures 4-5). The dislocation substructures differed subtly but clearly. RR had more well-formed first generation or non-crystallographic MBs, and the so-called random dislocation arrays or Taylor lattices appeared somewhat less random or more organized (Figure 6). These TEM observations were, arguably, qualitative and limited in statistics, but the difference in dislocation substructures appears convincing. Especially an argument (from our TEM observations) that RR somewhat encouraged the formation of DDWs and MBs, but these appeared less orientation sensitive, is in-tune with the mesoscopic EBSD measurements. It is to be noted that the special rolling techniques, with imposed redundant shear, had also shown remarkable tendencies for grain fragmentation. Especially, there are scattered references[18,27,50,94,95] on the imposition of reversible shear (or so-called changes in strain path) affecting grain fragmentation. Our study, on the other hand, has shown, and with direct experimental observations, that just an alteration of imposed shear direction has significant effects on the substructure evolution plus orientation sensitivity. Though our experimental observations appear conclusive, a definitive theoretical explanation remains pending. In the next paragraph, potential explanation(s) or approaches based on unproven (at least within the scope of the present study) theoretical possibilities are deliberated.

The changes in microstructures, as observed in the present study, can perhaps be approached through a continuum model or from CPFEM or discrete dislocation dynamics (DDD). For example, Taylor work or energy minimization [55,88] and textural softening[73,96] were related to relative stability of crystallographic orientations and grain fragmentation. Though this does not account for actual substructure formation, a continuum simulation has its intrinsic attraction and simplicity, and arguably may be used to incorporate the role of reversing shear. The CPFEM[93] may also capture the role of local shear on microstructure developments. Though even a full field CPFEM may require incorporation of strain gradients[97], with appropriate detailing on crystal plasticity, it has the potential for capturing microstructural changes with strain path or strain mode[18,86,87]. Finally, DDD incorporating aspects of dislocation movements from lower scale models[98,99] has shown the potential for bringing out all aspects of deformed microstructures, including role of solute and crystallographic orientations.

Our experiments on near boundary mesoscopic shear strain (NBMS) measurements (Figure 2), for example, revealed higher NBMS for the T0 grains of RR. As reported originally by Keskar et al.[64], NBMS often constitutes an important component of the overall strain matrix. For example, NBMS[64] was nearly one-order of magnitude higher than the actual plane strain compression of hexagonal zirconium. Further, the NBMS was shown to control the developments deformed microstructures, especially the grain fragmentation and in-grain misorientations. As the surface grain of RR were subjected to higher NBMS; they, arguably, developed stronger GND density and GROD. An alternate explanation might also emerge from dislocation dynamics[37]. For example, dislocations nucleate and move on respective slip planes. They interact at the intersection of the slip planes, forming junctions. The latter would lead to the creation of dynamic sources and obstacles. The reversal of dislocation movement (by reversing the shear or rolling direction) would, arguably, enhance the probability of junction formation; and might account for higher density of pinned dislocations[37]. In other words, explanations on the experimentally observed differences in GND and GROD might exist in the framework of both mechanics of local shear or NBMS and also dislocation dynamics. Though evolution of crystallographic textures were modelled quantitatively by systematically (and parametrically) varying local strain field, modelling the differences in deformed microstructures (with clear and statistically valid experimental observations – as offered in the present study) remains pending.

5. Conclusions

This study systematically used unidirectional (UDR) and reverse (RR) rolling to bring out the defining role of local or redundant shear on the as-rolled microstructure and texture evolution in the surface grains of both low and high solute bcc steel (IF and HSLA). Following are the main points emerging ,

1) Though surface grains of UDR and RR had identical strain and strain mode under macroscopic measurements, mesoscopically the imposition of local shear (especially, near boundary mesoscopic shear strains) appeared to differ noticeably. RR, in particular, had more mesoscopic local shear strain, especially in the low solute IF.
2) Surface grains in RR showed more GND density and misorientations. However, difference between the ideal crystallographic orientations and fibres were insignificant. These were observed in IF, but not in high solute HSLA. In particular, RR in IF appeared to encourage formation of well-defined dislocation boundaries (such as first-generation or non-crystallographic dense dislocation walls and micro bands), and even the random dislocation arrays (Taylor lattices) appeared more organized.
3) A clear gradient in experimental crystallographic textures were observed at different 'layers' of the as-rolled cross-sections of both IF and HSLA. Though mid-thickness textures were identical, there were noticeable differences in the surface (and sub-surface) textures. Using a parametric study of texture simulations (from a continuum

plasticity based binary-tree model) deformation textures were quantitatively modelled by introducing a location dependent strain field or local shear. In particular, local shear strains of UDR = +1.25 and RR= -0.85 were estimated, respectively, for the surface crystallographic textures of UDR and RR.

Acknowledgement

The authors would like to acknowledge support and collaboration from Defence Research and Development Organization DRDO ,India through the project (ERIP/ER/201612015/M/01/1732). Tata Steel and JSW are also acknowledged. Support from IITB Texture-OIM and TEM labs are also acknowledged.

CONFLICT OF INTEREST

The authors states that there is no conflict of interest.

Appendix

The texture predictions were based on the rate-independent binary-tree based continuum crystal plasticity simulation[55]. It was also found important to assume that the interfaces between interacting grains, and sub-aggregates in the binary-tree model, were perpendicular to ND. Plastic deformation was assumed to be accommodated by {110} <111> slip, and the critical resolved shear stress of all these slip systems was taken as constant throughout the simulation. The binary-tree based model of the polycrystal is based on dividing the aggregate of grains comprising the polycrystal into a pair of sub-aggregates. Each sub-aggregate (parent, p) is likewise further divided recursively into a pair of sub-aggregates (children, $c_1(p)$, and $c_2(p)$) until the smallest sub-aggregates are comprised of single grains. The boundary between $c_1(p)$, and $c_2(p)$ is assumed planar, with normal denoted by the unit vector $\nu(p)$. The binary-tree conceptualization of a four-grain 'polycrystal' is shown in Figure 8a. Two key features of the binary tree model are: (1) traction and velocity continuity across the sub-aggregate interfaces, i.e.,

$$(\sigma^{c_1(p)} - \sigma^{c_2(p)})\nu(p) = 0, \text{--(A1)}$$

and

$$(L^{c_1(p)} - L^{c_2(p)} = \lambda(p) \otimes \nu(p); \text{--(A2)}$$

and (2) the averaging of fields up the hierarchy of sub-aggregates:

$$\sigma^{(p)} = \ w^{c_1(p)}\sigma^{c_1(p)} + w^{c_2(p)}\sigma^{c_2(p)}, \text{---------------------------------(A3)}$$

and

$$L^{(p)} = \ w^{c_1(p)}L^{c_1(p)} + w^{c_2(p)}L^{c_2(p)}. \text{----------------------------------(A4)}$$

In these equations, σ, L, and w, denote the stress, velocity gradient, and volume fraction of the sub-aggregate indicated in their superscript. $\lambda(p)$ denotes the Hadamard characteristic segment, as detailed in by Mahesh[55].

Thus, grains in the binary tree model obey strict compatibility and traction continuity with their immediate neighbors and compatibility and traction continuity in a weaker (average) sense, with more distant neighbors. The model accounts for intergranular interactions, with these interactions becoming weaker with increasing distance between the interacting grains. The binary tree model is thus more refined than the full constraints Taylor model[89]. Further, as described in earlier studies[63,92,100,101], models like binary-tree are known to provide the most quantitative description of deformation texture developments. This has been shown in bcc steel and also in fcc aluminum. Alamel, for example, is capable of capturing the shear induced components of deformation texture, and captured deformation texture evolution as effectively as full-field crystal plasticity finite element. It is to be noted, that the binary tree model was effective in capturing shear texture components (including the minor ones) in the T0 sections of UDR and RR, respectively. The relevant data are given in Table S1 in supplementary material.

References

1 W.L. Roberts: *COLD ROLLING OF STEEL*, 1st Editio., Marcel Dekker,Inc, New York, Basel, 1978.

2 B. Verlinden, J. Driver, I. Samajdar, and R.D. Doherty: *Thermo-Mechanical Processing of Metallic Materials*, vol. 10, 10th edn., 2007.

3 T. Matsuoka and K. Yamamori: *METALLURGICAL TRANSACTIONS A*, 1975, vol. 6A, pp. 1613–22.

4 J. Pittner and M.A. Simaan: *Tandem Cold Metal Rolling Mill Control*, 1st edn., Springer London, London, 2011.

5 I.Ya.Tarnovskii, A.A.Pozdeyev, and V.B.Lyashkov: *Deformation of Metals during Rolling*, 1st edn., Pergamon Press Ltd., Oxford, 1965.

6 K. Komori and K. Koumura: *Journal of Materials Processing Technology*, 2000, vol. 105, pp. 24–31.

7 W. Soszyński and A. Studnicka: *A Review of Contemporary Solutions for Cold Rolling That Allow Quality Improvement Manufacturing and Processing*, 2012.

8 M. Glowacki: *Journal of Materials Processing Technology*, 2005, vol. 168, pp. 336–43.

9 A. V. Korznikov, Y. V. Ivanisenko, D. V. Laptionok, I.M. Safarov, V.P. Pilyugin, and R.Z. Valiev: *Nanostructured Materials*, 1994, vol. 4, pp. 159–67.

10 B. Verlinden: *Metallurgical and Materials Engineering*, 2018, pp. 165–82.

11 Y.T. Zhu and T.G. Langdon: *Jom*,2004, vol. 56, pp. 58-63.

12 W. Truszkowski, J. Kr'ol, and B. Major: *Metallurgical Transactions A*, 1980, vol. 11, pp. 749–58.

13 W. Truszkowski, J. Krol, and B. Major: *Metallurgical Transactions A*, 1982, vol. 13A, pp. 665–9.

14 C.S. Lee and B.J. Duggan: *Metallurgical Transactions A*, 1991, vol. 22, pp. 2637–43.

15 S.H. Lee and D.N. Lee: *International Journal of Mechanical Sciences*, 2001, vol. 43, pp. 1997–2015.

16 O. Engler, M.-Y. Huh, and C.N. Tomé: *Metallurgical and Materials Transactions A*, 2000, vol. 31A, pp. 2299–315.

17 O. V Mishin, B. Bay, and D. Juul Jensen: *Metallurgical and Materials Transactions A*, 2000, vol. 31A, pp. 1653–62.

18 N. Kamikawa, T. Sakai, and N. Tsuji: *Acta Materialia*, 2007, vol. 55, pp. 5873–88.

19 D.A. Hughes and N. Hansen: *Materials Science and Technology*, 2012, vol. 7, pp. 544–53.

20 E.F. Rauch and J.H. Schmitt: *Materials Science and Engineering A*, 1989, vol. 113, pp. 441–8.

21 S. Thuillier and E.F. Rauch: *Acta Metallurgica Et Materialia*, 1994, vol. 42, pp. 1973–83.

22 M.Y. Huht, O. Engler, and D. Raabe: :*Textures and Microstructures*, 1995, vol. 24, pp. 225-237.

23 B. Peeters, B. Bacroix, C. Teodosiu, P. Van Houtte, and E. Aernoudt: *Acta Materialia*, 2001, vol. 49, pp. 1621–32.

24 E. V. Nesterova, B. Bacroix, and C. Teodosiu: *Metallurgical and Materials Transactions A: Physical Metallurgy and Materials Science*, 2001, vol. 32, pp. 2527–38.

25 E. V Nesterova, B. Bacroix, and C. Teodosiu: *Materials Science and Engineering*, 2001, vol. 309, pp. 495–9.

26 E.F. Rauch, J.J. Gracio, F. Barlat, A.B. Lopes, and J. Ferreira Duarte: *Scripta Materialia*, 2002, vol. 46, pp. 881–6.

27 H. Fan, S. Liu, L. Li, C. Deng, and Q. Liu: *Materials and Design*, 2016, vol. 97, pp. 464–72.

28 J. Zhu, S. Liu, D. Long, Y. Liu, N. Lin, X. Yuan, and D. Orlov: *Journal of Materials Research and Technology*, 2020, vol. 9, pp. 4566–77.

29 N.P. Gurao, S. Sethuraman, and S. Suwas: *Metallurgical and Materials Transactions A: Physical Metallurgy and Materials Science*, 2013, vol. 44, pp. 1497–507.

30 A. Ghosh, A. Singh, and N.P. Gurao: *Materials Characterization*, 2017, vol. 125, pp. 83–93.

31 S. Wronski and B. Bacroix: *Materials Characterization*, 2016, vol. 118, pp. 235–43.

32 N.P. Gurao, A. Ali A, and S. Suwas: *Materials Science and Engineering A*, 2009, vol. 504, pp. 24–35.

33 H. Wang, C. Lu, and K. Tieu: *Crystals*, 2019, vol. 9, pp. 1–10.

34 R.K. Sabat, P.K. Samal, and M. Ahamed S: *Materials Science and Engineering A*, 2018, vol. 715, pp. 348–58.

35 Z. Zhang, D. Chen, H. Zhao, and S. Liu: *International Journal of Refractory Metals and Hard Materials*, 2013, vol. 41, pp. 453–60.

36 S.K. Sahoo, R.K. Sabat, B.D. Bishoyi, A.G.S. Anjani, and S. Suwas: *Materials Letters*, 2016, vol. 180, pp. 166–9.

37 A. Prakash, T.N. Tak, A. Anand, N.N. Pai, S.V.S. Narayana Murty, C.V. Singh, P.J. Guruprasad, and I. Samajdar: *Metallurgical and Materials Transactions A*, 2022, pp. 1–19.

38 S.K. Sahoo, V.D. Hiwarkar, P. Pant, I. Samajdar, K. V. ManiKrishna, G.K. Dey, D. Srivastav, R. Tewari, and S. Banerjee: *Materials Science Forum*, 2012, vol. 702–703, pp. 838–41.

39 M. Matsuo, T. Sakai, and Y. Suga: *Metallurgical Transactions A*, 1986, vol. 17, pp. 1313–22.

40 S.E. Schoenfeld and R.J. Asaro: *International Journal of Mechanical Sciences*, 1996, vol. 38, pp. 661–83.

41 S.S. Dhinwal and L.S. Toth: *Materials Characterization*, 2020, vol. 169, p. 17.

42 B. Hutchinson: *Philosophical Transactions of the Royal Society A: Mathematical, Physical and Engineering Sciences*, 1999, vol. 357, pp. 1471–85.

43 P. Van Houtte, L. Delannay, and I. Samajdar: *Textures and Microstructures*, 1999, vol. 31, pp. 109-149.

44 J. Sidor, A. Miroux, R. Petrov, and L. Kestens: *Acta Materialia*, 2008, vol. 56, pp. 2495–507.

45 M.Y. Huh, H.C. Kim, J.J. Park, and O. Engler: *Metals and Materials International*, 1999, vol. 5, pp. 437–43.

46 Y.B. Xu, Y.L. Bai, Q. Xue, and L.T. Shen: *Acta Materialia*, 1996, vol. 44, pp. 1917–26.

47 R. Roumina and C.W. Sinclair: *Metallurgical and Materials Transactions A: Physical Metallurgy and Materials Science*, 2008, vol. 39, pp. 2495–503.

48 P. Blandford, J.A. Szpunar, D. Daniel, and J.J. Jonas: *Textures and Microstructures*, 1991, vol. 14-18, pp. 525-530.

49 T. Clausmeyer, G. Gerstein, S. Bargmann, B. Svendsen, A.H. Van Den Boogaard, and B. Zillmann: *Journal of Materials Science*, 2013, vol. 48, pp. 674–89.

50 D. V Wilson and P.S. Bate: ~ *Pergamon Acta metall, mater*, 1994, vol. 42, pp. 1099–111.

51 J.Y. Kang, B. Bacroix, H. Réglé, K.H. Oh, and H.C. Lee: *Acta Materialia*, 2007, vol. 55, pp. 4935–46.

52 N. Hansen: *Scripta Metallurgica et Materiala*, 1992, vol. 27, pp. 1447–52.

53 K. Shen and B.J. Duggan: *Acta Materialia*, 2007, vol. 55, pp. 1137–44.

54 Q.Z. Chen, M.Z. Quadir, and B.J. Duggan: *Philosophical Magazine*, 2006, vol. 86, pp. 3633–46.

55 S. Mahesh: *International Journal of Plasticity*, 2010, vol. 26, pp. 42–64.

56 F. Bachmann, R. Hielscher, and H. Schaeben: in *Solid State Phenomena*, vol. 160, Trans Tech Publications Ltd, 2010, pp. 63–8.

57 P. Van Houtte: Manuals MTM-FHM, Department of Metallurgy and Materials Engineering – KU Leuven, Belgium 1995.

58 H.-J. Bunge: *H-J Bunge*, Butterworth & Co, 1982.

59 U. Welzel, J. Ligot, P. Lamparter, A.C. Vermeulen, and E.J. Mittemeijer: *Journal of Applied Crystallography*, 2005, 38, vol. 38.

60 P.S. Prevey: *X-RAY DIFFRACTION RESIDUAL STRESS TECHNIQUES*, 1986.

61 P.J. Withers and H.K.D.H. Bhadeshia: *Materials Science and Technology*, 2001, vol. 17, pp. 355–65.

62 K. V. Mani Krishna, R. Raghavan, D. Srivastava, G.K. Dey, S.K. Sahoo, and I. Samjdar: *Transactions of the Indian Institute of Metals*, 2011, vol. 64, pp. 309–13.

63 S. Raveendra, A.K. Kanjarla, H. Paranjape, S.K. Mishra, S. Mishra, L. Delannay, I. Samajdar, and P. Van Houtte: *Metallurgical and Materials Transactions A: Physical Metallurgy and Materials Science*, 2011, vol. 42, pp. 2113–24.

64 N. Keskar, S. Mukherjee, K. V. Mani Krishna, D. Srivastava, G.K. Dey, P. Pant, R.D. Doherty, and I. Samajdar: *Acta Materialia*, 2014, vol. 69, pp. 265–74.

65 J. Singh, S. Mahesh, G. Kumar, P. Pant, D. Srivastava, G.K. Dey, N. Saibaba, and I. Samajdar: *Metallurgical and Materials Transactions A*, 2015, vol. 46, pp. 5058–71.

66 T.J. Ruggles and D.T. Fullwood: *Ultramicroscopy*, 2013, vol. 133, pp. 8–15.

67 I. Samajdar and P. Van Houtte: *Acta Materialia*, 1998, vol. 46, pp. 2751–63.

68 I. Samajdar, B. Verlinden, L. Kestens, and P. Van Houtte: *Acta Materialia*, 1998, vol. 47, pp. 55–65.

69 W.B. Hutchinson: *International Metals Reviews*, 1984, vol. 29, pp. 25–42.

70 P.S. Bate and J. Quinta da Fonseca: *Materials Science and Engineering A*, 2004, vol. 380, pp. 365–77.

71 S. Li, I.J. Beyerlein, and M.A.M. Bourke: *Materials Science and Engineering A*, 2005, vol. 394, pp. 66–77.

72 R. Khatirkar, K. V Mani Krishna, L.A.I. Kestens, R. Petrov, P. Pant, and I. Samajdar: *ISIJ International*, 2011, vol. 51, pp. 849–56.

73 R. Khatirkar, B. Vadavadagi, Satish, K. Shekhawat, A. Haldar, and I. Samajdar: *ISIJ International*, 2012, vol. 52, pp. 884–93.

74 I. Samajdar, B. Verlinden, P. Van Houtte, and D. Vanderschueren: *Materials Science and Engineering*, 1997, vol. 238, pp. 343–50.

75 R. Khatirkar, B. Vadavadagi, A. Haldar, and I. Samajdar: *ISIJ International*, 2012, vol. 52, pp. 894–901.

76 L.S. Toth, J.J. Jonas, D. Daniel, and R.K. Ray: *Metallurgical Transactions A*, 1990, vol. 21A, pp. 2985–3000.

77 R.K. Ray, J.J. Jonas, and R.E. Hook: *International Materials Review*, 1994, vol. 39, pp. 129–72.

78 M. Hoelscher, D. Raabe, and K. Luecke: *Steel Research*, 1991, vol. 62, pp. 567–75.

79 K.H.H. Ahmed and A. Ihsan: *Advances in Physics Theories and Applications*, 2015, vol. 49, pp. 46–56.

80 A. Lodh, T.N. Tak, A. Prakash, P.J. Guruprasad, S.M. Keralavarma, A.A. Benzerga, C. Hutchinson, and I. Samajdar: *Metallurgical and Materials Engineering*, 2019, vol. 50, pp. 5038–55.

81 B.L. Li, A. Godfrey, Q.C. Meng, Q. Liu, and N. Hansen: *Acta Materialia*, 2004, vol. 52, pp. 1069–81.

82 X. Huang and G. Winther: *Philosophical Magazine*, 2007, vol. 87, pp. 5189–214.

83 Q.Z. Chen and B.J. Duggan: *Metallurgical and Materials Transactions A: Physical Metallurgy and Materials Science*, 2004, vol. 35 A, pp. 3423–30.

84 S. Suwas and R.K. Ray: *Deformation Textures*, Springer, Brian Derby, Manchester, UK, 2014.

85 P. Van Houtte, L. Delannay, and S.R. Kalidindi: *International Journal of Plasticity*, 2002, vol. 18, pp. 359–77.

86 H. Wang, C. Lu, and R. Wang: *International Journal of Advanced Manufacturing Technology*, 2020, vol. 111, pp. 37–51.

87 D.C. Camilo Magalhães, O.M. Cintho, J.B. Rubert, V.L. Sordi, and A.M. Kliauga: *Materials Science and Engineering A*, 2020,vol. 796, 140055.

88 S. Mahesh: *International Journal of Plasticity*, 2009, vol. 25, pp. 752–67.

89 T.G. I.: *J. Inst. Metals*, 1938, vol. 62, pp. 307–24.

90 A. Molinari, G.R. Canova, and S. Ahzi: *Acta metall*, 1987, vol. 35, pp. 2983–94.

91 U.F. Kocks' and H. Chandra: *Acta Materialia*, 1982, vol. 30, pp. 695–709.

92 P. Van Houtte, S. Li, M. Seefeldt, and L. Delannay: *International Journal of Plasticity*, 2005, vol. 21, pp. 589–624.

93 Y. Wu, Y. Shen, K. Chen, Y. Yu, G. He, and P. Wu: *Journal of Alloys and Compounds*, 2017, vol. 711, pp. 495–505.

94 Z.J. Li, G. Winther, and N. Hansen: *Acta Materialia*, 2006, vol. 54, pp. 401–10.

95 N.A. Sakharova and J. V. Fernandes: *Materials Chemistry and Physics*, 2006, vol. 98, pp. 44–50.

96 S. Cicalè, I. Samajdar, B. Verlinden, G. Abbruzzese, and P. Van Houtte: *ISIJ International*, 2002, vol. 42, pp. 770–8.

97 S. Zaefferer, J.C. Kuo, Z. Zhao, M. Winning, and D. Raabe: *Acta Materialia*, 2003, vol. 51, pp. 4719–35.

98 A. Lodh, T.N. Tak, A. Prakash, P.J. Guruprasad, C. Hutchinson, and I. Samajdar: *Metallurgical and Materials Transactions A: Physical Metallurgy and Materials Science*, 2017, vol. 48, pp. 5317–31.

99 A. Lodh, U. Tewary, R.P. Singh, T.N. Tak, A. Prakash, A. Alankar, P.J. Guruprasad, and I. Samajdar: *Metallurgical and Materials Transactions A*, 2018, vol. 49, pp. 5946–52.

100 A.A. Saleh, C. Haase, E. V. Pereloma, D.A. Molodov, and A.A. Gazder: *Acta Materialia*, 2014, vol. 70, pp. 259–71.

101 T. Leffers and D.J. Jensen: *Textures and Microstructures*, 1986, vol. 6, pp. 231–63.